Article

Neuron

Presenilin-1 Knockin Mice Reveal Loss-of-Function Mechanism for Familial Alzheimer's Disease

Highlights

- FAD-linked *Presenilin-1* mutations cause complete loss of PS1 function in vivo
- FAD-linked *Presenilin-1* mutations abolish γ-secretase activity
- FAD-linked *Presenilin-1* mutations impair hippocampal memory and synaptic function
- FAD-linked *Presenilin-1* mutations cause age-dependent neurodegeneration

Authors

Dan Xia, Hirotaka Watanabe, ..., Jie Shen, Raymond J. KelleherIII

Correspondence

jshen@rics.bwh.harvard.edu (J.S.), kelleher@helix.mgh.harvard.edu (R.J.K.)

In Brief

How Presenilin mutations cause Alzheimer's disease is a key unresolved problem. Xia et al. show, unexpectedly, that such mutations cause AD-like symptoms in mice through a loss-of-function mechanism, suggesting that restoring Presenilin function may be a promising therapeutic strategy.

Xia et al., 2015, Neuron *85*, 967–981
March 4, 2015
http://dx.doi.org/10.1016/j.neuron.2015.02.010

CellPress

Neuron
Article

Presenilin-1 Knockin Mice Reveal Loss-of-Function Mechanism for Familial Alzheimer's Disease

Dan Xia,[1,2] Hirotaka Watanabe,[1] Bei Wu,[1] Sang Hun Lee,[1] Yan Li,[3] Evgeny Tsvetkov,[3] Vadim Y. Bolshakov,[3,4] Jie Shen,[1,4,5,*] and Raymond J. Kelleher III[2,4,5,*]

[1]Center for Neurologic Diseases, Department of Neurology, Brigham & Women's Hospital, Harvard Medical School, Boston, MA 02115, USA
[2]Center for Human Genetic Research, Department of Neurology, Massachusetts General Hospital, Harvard Medical School, Boston, MA 02114, USA
[3]Department of Psychiatry, McLean Hospital, Harvard Medical School, Belmont, MA 02478, USA
[4]Program in Neuroscience, Harvard Medical School, Boston, MA 02115, USA
[5]Co-senior author
*Correspondence: jshen@rics.bwh.harvard.edu (J.S.), kelleher@helix.mgh.harvard.edu (R.J.K.)
http://dx.doi.org/10.1016/j.neuron.2015.02.010

SUMMARY

Presenilins play essential roles in memory formation, synaptic function, and neuronal survival. Mutations in the *Presenilin-1* (*PSEN1*) gene are the major cause of familial Alzheimer's disease (FAD). How *PSEN1* mutations cause FAD is unclear, and pathogenic mechanisms based on gain or loss of function have been proposed. Here, we generated *Psen1* knockin (KI) mice carrying the FAD mutation L435F or C410Y. Remarkably, KI mice homozygous for either mutation recapitulate the phenotypes of *Psen1*$^{-/-}$ mice. Neither mutation altered *Psen1* mRNA expression, but both abolished γ-secretase activity. Heterozygosity for the KI mutation decreased production of Aβ40 and Aβ42, increased the Aβ42/Aβ40 ratio, and exacerbated Aβ deposition. Furthermore, the L435F mutation impairs hippocampal synaptic plasticity and memory and causes age-dependent neurodegeneration in the aging cerebral cortex. Collectively, our findings reveal that FAD mutations can cause complete loss of Presenilin-1 function in vivo, suggesting that clinical *PSEN* mutations produce FAD through a loss-of-function mechanism.

INTRODUCTION

Dominant mutations in the *PSEN1* and *PSEN2* genes encoding Presenilin-1 (PS1) and Presenilin-2 (PS2) are the major cause of familial Alzheimer's disease, and more than 200 distinct causative mutations distributed throughout the coding sequences have been identified (http://www.alzforum.org/mutations). Presenilin (PS) comprises the catalytic component of γ-secretase (Li et al., 2000), which carries out intramembranous cleavage of type I transmembrane proteins, including the amyloid precursor protein (APP) and Notch receptors (De Strooper et al., 1999; Song et al., 1999; Struhl and Greenwald, 1999). *Psen1* null mice display perinatal lethality with developmental defects and impaired neurogenesis attributable to loss of Notch signaling activity (Handler et al., 2000; Shen et al., 1997), whereas *Psen2* null mice have no detectable brain phenotypes (Saura et al., 2004; Steiner et al., 1999). In the adult brain, Presenilins play essential roles in synaptic function, learning and memory, and neuronal survival (Saura et al., 2004; Wines-Samuelson et al., 2010; Yu et al., 2001; Zhang et al., 2009, 2010).

Despite these insights into PS function in the brain, the mechanism by which *PSEN* mutations lead to neurodegeneration and dementia in FAD remains a key unresolved issue. Both gain-of-function (Hardy and Selkoe, 2002) and loss-of-function (Shen and Kelleher, 2007) pathogenic mechanisms have been proposed. FAD mutations in *PSEN* have been reported to increase Aβ42 production selectively, suggesting that *PSEN* mutations may cause FAD via increased Aβ42/Aβ40 ratio (Borchelt et al., 1996; Duff et al., 1996; Scheuner et al., 1996). However, FAD patients carrying *PSEN* mutations develop the disease at a significantly earlier age of onset, relative to APP mutations (Ryman et al., 2014), even though the increase in the Aβ42/Aβ40 ratio conferred by *PSEN* mutations is typically rather small. Furthermore, overproduction of Aβ including Aβ42 has failed to produce significant neurodegeneration in mice (Games et al., 1995; Hsiao et al., 1996; Mucke et al., 2000), suggesting that Aβ42 overproduction itself may be insufficient to initiate neurodegeneration. Surprisingly, conditional inactivation of Presenilins (Beglopoulos et al., 2004; Saura et al., 2004; Wines-Samuelson et al., 2010) or another component of the γ-secretase complex Nicastrin (Tabuchi et al., 2009) in the adult mouse brain produced widespread neurodegeneration, inflammation, and tau hyperphosphorylation, raising the possibility that *PSEN* mutations may cause neurodegeneration and dementia in FAD via a loss of essential PS functions.

Using a sensitive cell-based assay system, we found that a series of clinical *PSEN1* mutations uniformly impaired γ-secretase activity with the L435F and C410Y mutations causing virtually complete loss of γ-secretase-dependent processing of APP and Notch (Heilig et al., 2010, 2013). These findings raised the pivotal question of whether FAD mutations cause a loss of PS function in vivo, and whether loss of PS function by clinical mutations can trigger key AD-related phenotypes. To address these questions, we introduced the L435F or C410Y mutation into the

genomic *Psen1* locus and analyzed their impact on PS1 function and γ-secretase activity in the developing and adult brain. Strikingly, both the L435F and C410Y mutations yielded null alleles in vivo, as knockin (KI) mice homozygous for either mutation displayed morphological, neurodevelopmental, and biochemical phenotypes indistinguishable from those of *Psen1* null mice. Moreover, replacement of a wild-type *Psen1* allele with the L435F KI allele in adult mice produced a series of neuropathological, synaptic, and behavioral changes relevant to FAD, including elevation of the Aβ42/Aβ40 ratio and accelerated Aβ deposition in a human *APP* transgenic background, impaired hippocampal synaptic plasticity and memory, and cerebral cortical neurodegeneration. Collectively, these findings support the hypothesis that loss of PS essential functions plays an important role in FAD pathogenesis.

RESULTS

FAD Mutations L435F and C410Y Preserve *Psen1* mRNA Expression but Reproduce *Psen1* Null Phenotypes In Vivo

To determine the impact of FAD mutations in vivo, we generated two independent KI mice in which the FAD-linked L435F or C410Y mutation was introduced into the genomic *Psen1* locus. The L435F mutation was identified in early-onset FAD with cerebral cotton wool plaque neuropathology (Heilig et al., 2010; Rogaeva et al., 2001). The C410Y substitution was one of the first five FAD mutations reported in *PSEN1* (Sherrington et al., 1995) and has been extensively characterized, including its association with cerebral cotton wool plaques (Haleem et al., 2007; Klunk et al., 2007; Moonis et al., 2005). The L435F or C410Y missense mutation was introduced into *Psen1* exon 12 or 11, respectively, by homologous recombination (Figure 1A) and further verified by Southern analysis and sequencing (Figures S1A–S1C).

Strikingly, homozygous $Psen1^{L435F/L435F}$ (L435F KI/KI) and $Psen1^{C410Y/C410Y}$ (C410Y KI/KI) mice display developmental abnormalities indistinguishable from the phenotypes observed in $Psen1^{-/-}$ mice (Shen et al., 1997), including perinatal lethality, shortened rostro-caudal body axis, and shortened, kinked tails (Figure 1B; Table S1). To determine whether introduction of the FAD mutation disrupts *Psen1* expression, we examined *Psen1* mRNA levels in L435F and C410Y KI/KI, KI/+, and $Psen1^{+/+}$ brains at postnatal day 0 (P0). In contrast to the absence of *Psen1* mRNA in $Psen1^{-/-}$ mice (Shen et al., 1997), northern analysis showed normal levels of full-length *Psen1* mRNA in KI/KI brains (Figure 1C). Western analysis revealed drastically reduced levels of endoproteolytically processed PS1 N- and C-terminal fragments (NTFs and CTFs) in KI/KI brains and corresponding accumulation of PS1 holoprotein in a KI allele dosage-dependent manner (Figure 1D). Thus, the L435F and C410Y mutations do not affect *Psen1* mRNA expression but abolish the normal presenilinase activity of PS1. To assess whether the L435F mutation affects the expression of γ-secretase complex components, we measured levels of Nicastrin and Pen-2 and found that they are similar in $Psen1^{+/+}$, L435F KI/KI, and KI/+ brains but significantly reduced in $Psen1^{-/-}$ brains (Figure S1D), suggesting that PS1 holoprotein with the L435F mutation is sufficient to maintain normal levels of other γ-secretase components, despite the drastic reduction of PS1 NTFs and CTFs.

Impaired Notch Signaling and Neurogenesis in L435F and C410Y KI/KI Mice

Presenilin is required for the proteolytic cleavage of Notch to release its intracellular effector domain (NICD) (Struhl and Greenwald, 1999). We assessed Notch signaling activity using an in vitro assay for de novo NICD production and found that NICD production is markedly reduced in L435F and C410Y KI/+ brains and largely eliminated in KI/KI brains (Figure 2A). Northern analysis revealed that levels of the Notch effector gene *Hes5* are decreased in L435F and C410Y KI/KI brains to a similar extent as those in $Psen1^{-/-}$ brains (Figure 2B). These data provide further confirmation that the L435F and C410Y KI mutations impair Notch signaling.

Inactivation of PS1 function causes neural developmental defects, including depletion of neural progenitor cells and impaired neurogenesis (Handler et al., 2000; Kim and Shen, 2008; Shen et al., 1997). We therefore evaluated the impact of the L435F and C410Y mutations on brain development. Similar to $Psen1^{-/-}$ mice (Handler et al., 2000; Shen et al., 1997), L435F and C410Y KI/KI mice display pronounced thinning of the ventricular zones within the lateral ganglionic eminence and developing telencephalon at embryonic day 16.5 (E16.5) compared to littermate $Psen1^{+/+}$ mice (Figure 2C). Moreover, the number of proliferating cells detected by Ki67 immunoreactivity is significantly reduced in the ventricular zone of L435F and C410Y KI/KI brains (Figure 2D). These phenotypes bear striking resemblance to those in $Psen1^{-/-}$ mice (Shen et al., 1997), further indicating that the effects of the L435F and C410Y mutations on neurodevelopment and γ-secretase-mediated cleavage of Notch are comparable to the null mutation.

Inactivation of γ-Secretase by the L435F and C410Y Mutations

To investigate further the impact of the L435F and C410Y mutations on γ-secretase activity, we examined proteolytic processing of APP. Western analysis revealed that APP CTFs, the direct substrate of γ-secretase, accumulate to a similar extent in L435F and C410Y KI/KI mice and $Psen1^{-/-}$ mice, indicating comparable deficiencies in γ-secretase activity (Figure 3A; Figure S2A). We next analyzed γ-secretase activity using an in vitro assay for de novo Aβ production (Takahashi et al., 2003; Watanabe et al., 2012) and found that production of Aβ40 and Aβ42 is absent in KI/KI brains and markedly reduced in KI/+ brains for each mutation (Figure 3B; Figure S2B). We also measured the steady-state levels of endogenous mouse Aβ directly from brain homogenates. Strikingly, endogenous Aβ40 and Aβ42 are undetectable in KI/KI brains, whereas Aβ40 and Aβ42 levels in KI/+ embryonic brains are similar to those in $Psen1^{+/+}$ brains for each mutation (Figure 3C; Figure S2C). N-Cadherin CTF1, another γ-secretase substrate (Marambaud et al., 2003), also displayed significant accumulation in L435F and C410Y KI/KI as well as $Psen1^{-/-}$ brains (Figure S2D). These results demonstrate that the L435F and C410Y mutations disrupt γ-secretase activity to an extent comparable to complete loss of PS1 function.

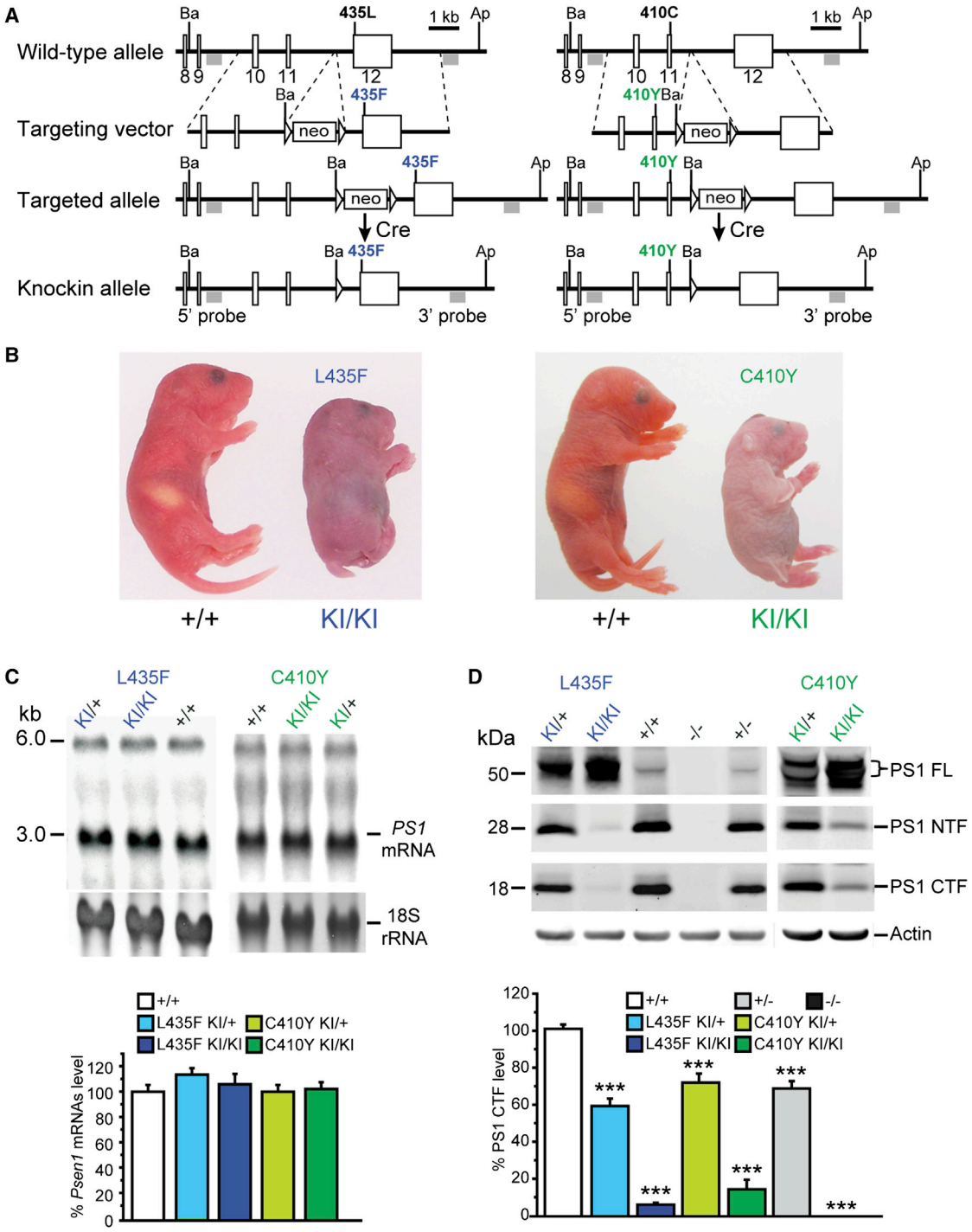

Figure 1. L435F and C410Y KI/KI Mice Exhibit Phenotypes Indistinguishable from *Psen1*$^{-/-}$ Mice

(A) Targeting strategy for the generation of L435F and C410Y KI mice. Boxes represent *Psen1* exons 8–12, and the locations of the 5′ and 3′ external probes are shown. The L435F mutation is located in exon 12, and C410Y mutation is located in exon 11. Ba and Ap denote BamHI and *Apa*I restriction sites, respectively.

(B) Newborn L435F and C410Y KI/KI pups resemble *Psen1*$^{-/-}$ pups with shortened tail and rostrocaudal body axis.

(C) Northern analysis of brain total RNA at P0 shows normal *Psen1* mRNA size and level in L435F and C410Y KI/KI and KI/+ mice ($n \geq 5$).

(D) Western analysis of brain lysates at P0 shows residual amounts of PS1 NTFs and CTFs in L435F and C410Y KI/KI brains and drastic accumulation of PS1 holoprotein in L435F and C410Y KI/KI and KI/+ brains in a KI gene dosage-dependent manner, whereas these PS1 species are undetectable in *Psen1*$^{-/-}$ brains ($n \geq 4$). Data are represented as mean ± SEM. ***$p < 0.001$.

See also Figure S1 and Table S1.

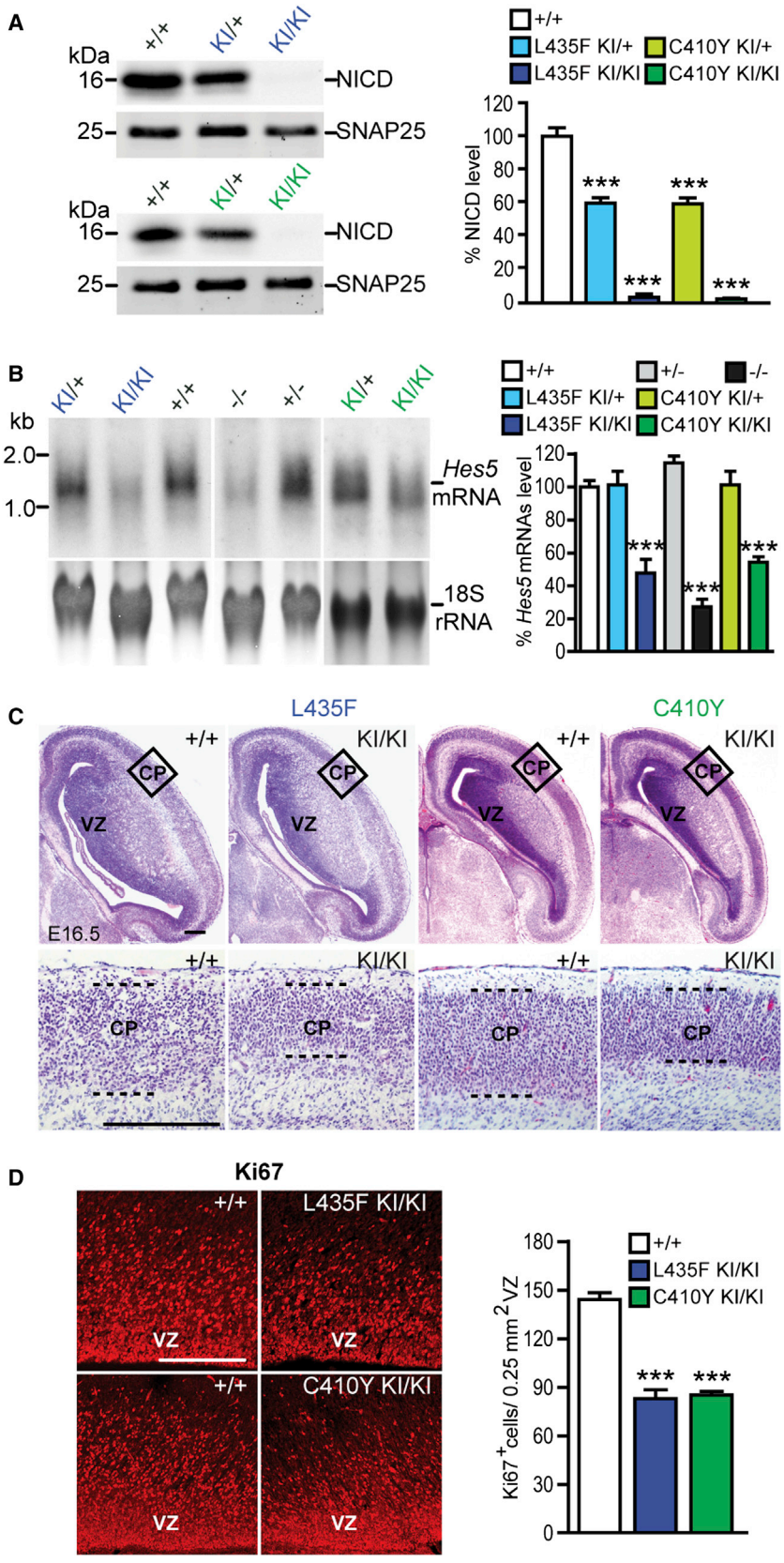

Figure 2. Impaired Neurogenesis and Notch Signaling in L435F and C410Y KI/KI Mice

(A) In vitro γ-secretase assay using CHAPSO-solubilized E18.5 brain fractions and recombinant Notch substrate N102-FmH followed by western analysis reveals that NICD production is reduced in L435F KI/+ (n = 3) and C410Y KI/+ (n = 4) mice and abolished in L435F KI/KI (n = 3) and C410Y KI/KI (n = 3) mice compared to *Psen1*$^{+/+}$ controls (n = 6). SNAP25 is used as internal loading control for membrane fractions.

(B) Northern analysis of *Hes5* expression. Levels of *Hes5* mRNA are markedly reduced in L435F KI/KI (n = 9), C410Y KI/KI (n = 3), *Psen1*$^{-/-}$ (n = 3) brains relative to *Psen1*$^{+/+}$ controls (n = 7).

(C) H&E staining of comparable brain sections from L435F KI/KI, C410Y KI/KI, and littermate controls at E16.5 shows that the ventricular zone (VZ) and the developing cortical plate (CP) are thinner in L435F KI/KI and C410Y KI/KI mice. The bottom panels show higher-power views of the boxed areas in the developing CP. Dashed lines show the boundaries of the CP. Scale bar, 0.25 mm.

(D) The number of proliferating neural progenitor cells in the VZ labeled by Ki67 immunoreactivity is reduced in L435F KI/KI and C410Y KI/KI brains at E16.5 (n = 4 for each genotype). Scale bar, 0.25 mm. Data are represented as mean ± SEM. ***p < 0.001.

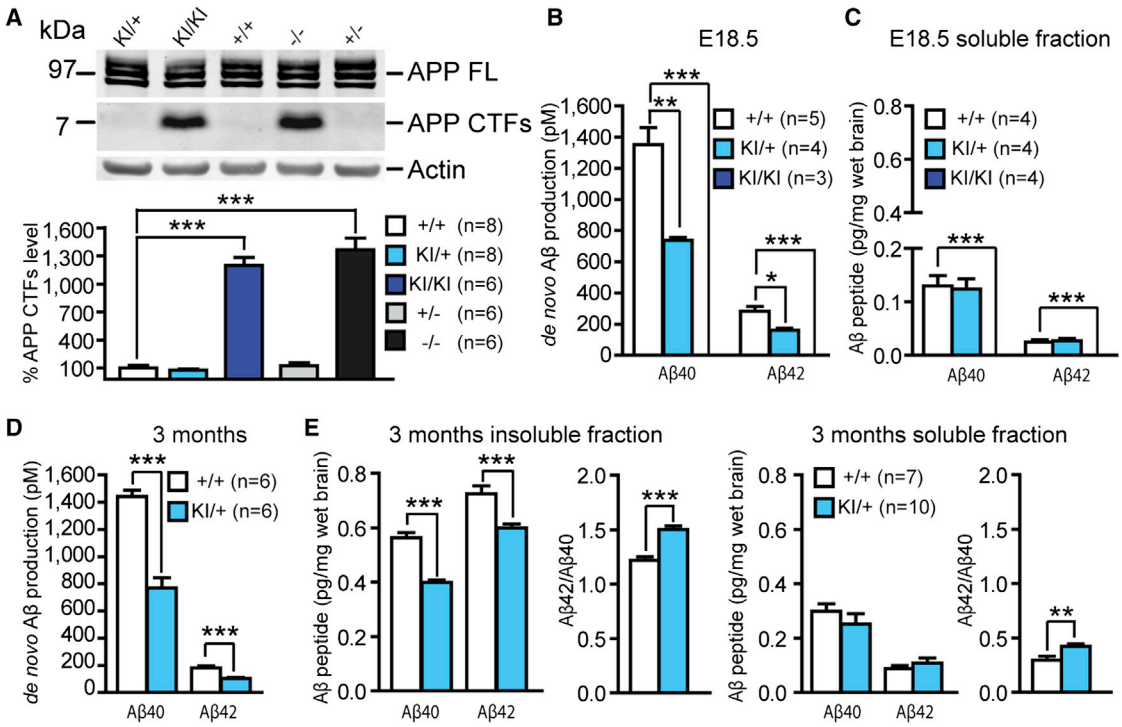

Figure 3. Abolished Aβ Production in L435F KI/KI Mice and Reduced Aβ40 and Aβ42 Production in L435F KI/+ Mice

(A) APP CTFs accumulate (>10-fold) in L435F KI/KI and *Psen1*$^{-/-}$ brains relative to littermate controls at E18.5 (n ≥ 6).

(B) ELISA measurements of Aβ40 and Aβ42 following in vitro γ-secretase assay. In vitro γ-secretase assay reveals that de novo generation of Aβ40 and Aβ42 in L435F KI/+ brains at E18.5 (n = 4) is reduced by 46% and 43%, respectively, compared to *Psen1*$^{+/+}$ brains (n = 5), and they are undetectable in L435F KI/KI brains (n = 3).

(C) ELISA measurements of endogenous Aβ40 and Aβ42 from brain homogenates at E18.5. Levels of stead-state endogenous Aβ40 and Aβ42 are similar between L435F KI/+ and *Psen1*$^{+/+}$ brains, and they are undetectable in L435F KI/KI brains (n = 4 for each genotype).

(D) ELISA measurements of Aβ40 and Aβ42 following in vitro γ-secretase assay in 3-month-old mice. De novo generation of Aβ40 and Aβ42 in L435F KI/+ cortical homogenates is reduced by 47% and 43%, respectively, compared to *Psen1*$^{+/+}$ cortices (n = 6 for each genotype).

(E) ELISA measurements of steady-state endogenous Aβ40 and Aβ42 in both insoluble and soluble fractions from cortical samples at 3 months of age. In insoluble fractions, levels of endogenous Aβ40 and Aβ42 are reduced in L435F KI/+ cortices (n = 10) relative to controls (n = 7), and the Aβ42/Aβ40 ratio is increased. In soluble fractions, levels of endogenous Aβ40 and Aβ42 are not significantly different between *Psen1*$^{L435F/+}$ and *Psen1*$^{+/+}$ cortices, but the Aβ42/Aβ40 ratio is significantly increased in *Psen1*$^{L435F/+}$ cortices. Data are represented as mean ± SEM. *p < 0.05; **p < 0.01; ***p < 0.001.

See also Figure S2 and Table S2.

Reduction of Aβ40 and Aβ42 Production and Elevation of the Aβ42/Aβ40 Ratio in Adult KI/+ Brains

Although L435F KI/KI mice exhibit perinatal lethality, L435F KI/+ mice are viable and fertile. Notably, L435F KI/+ mice provide a precise genetic animal model of the *PSEN1* mutation in FAD. To determine how the L435F mutation affects Aβ production in the adult brain, we performed in vitro assay using L435F KI/+ and littermate *Psen1*$^{+/+}$ mice at 3 months of age. Levels of de novo Aβ40 and Aβ42 production in L435F KI/+ mice are reduced to approximately half of those in *Psen1*$^{+/+}$ mice (Figure 3D). We next measured steady-state levels of endogenous Aβ40 and Aβ42 in both insoluble and soluble fractions from the cerebral cortex at 3 months of age. In insoluble fractions, levels of Aβ40 and Aβ42 are significantly reduced (by 29% and 17%, respectively), and the Aβ42/Aβ40 ratio is correspondingly increased (~15%) in L435F KI/+ mice (Figure 3E). In soluble fractions, levels of Aβ40 and Aβ42 are lower than those in insoluble fractions and not significantly altered, but the ratio of Aβ42/Aβ40 is elevated in L435F KI/+ mice compared to that in *Psen1*$^{+/+}$ mice (Figure 3E). These results show that heterozygosity for the L435F mutation elevates the Aβ42/Aβ40 ratio due to a greater reduction in accumulation of Aβ40 relative to Aβ42.

The L435F KI Mutation Exacerbates Aβ Plaque Deposition in Human Mutant *APP* Transgenic Mice

To investigate how the loss of PS1 function conferred by the L435F mutation affects human Aβ production and plaque formation, we crossed L435F KI/+ mice to transgenic mice overexpressing human wild-type (*APP*^{WT}, I5 line) or mutant (*APP*^{MT}, J20 line) APP (Mucke et al., 2000) in which Aβ40 and Aβ42 are dramatically overproduced (Table S2). We first measured levels of human Aβ40 and Aβ42 in insoluble and soluble fractions from the cerebral cortex of *Psen1*$^{L435F/+}$; *APP*^{WT} and *Psen1*$^{+/+}$; *APP*^{WT} mice at 9 months of age (Figure 4A). In *Psen1*$^{L435F/+}$; *APP*^{WT} mice, steady-state levels of human Aβ40 and Aβ42 are significantly reduced in insoluble fractions, and the Aβ42/Aβ40

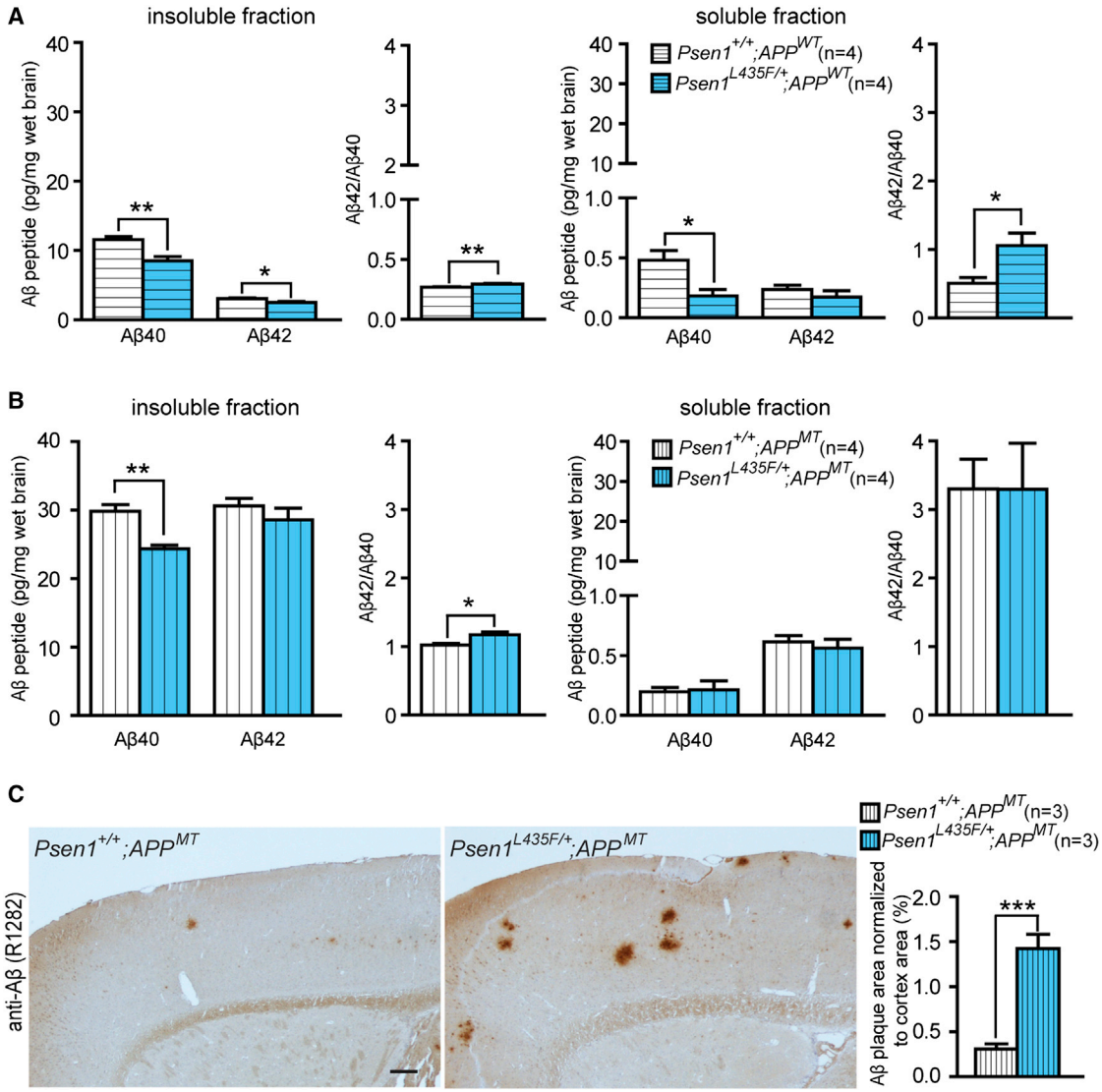

Figure 4. Reduced Human Aβ Accumulation, but Accelerated Amyloid Deposition in L435F KI/+ Mice Expressing a Human Mutant *APP* Transgene

(A) ELISA measurements of steady-state human Aβ40 and Aβ42 in insoluble and soluble fractions from *Psen1*$^{L435F/+}$; *APP*^{WT} (n = 4) and controls (n = 4) at 9 months of age. In *Psen1*$^{L435F/+}$; *APP*^{WT} mice, human Aβ40 is reduced by ~26% in insoluble fractions and ~62% in soluble fractions, whereas human Aβ42 is reduced by ~19% in insoluble fractions, but is not significantly changed in soluble fractions. Note that levels of Aβ40 and Aβ42 are much higher in insoluble fractions than in soluble fractions (>20-fold for Aβ40, >10-fold for Aβ42). The Aβ42/Aβ40 ratio is significantly enhanced in soluble and insoluble fractions.

(B) ELISA measurements of steady-state human Aβ40 and Aβ42 in insoluble and soluble fractions of cortical homogenates from *Psen1*$^{+/+}$; *APP*^{MT} (n = 4) and *Psen1*$^{L435F/+}$; *APP*^{MT} (n = 4) at 2 months of age. Levels of human Aβ40 are significantly reduced in insoluble fractions, but not in soluble fractions, whereas levels of human Aβ42 are not significantly altered. Note that levels of Aβ40 are drastically higher in insoluble fractions than in soluble fractions (>100-fold). The Aβ42/Aβ40 ratio is significantly increased in insoluble fractions.

(C) Aβ immunostaining with an Aβ antibody (R1282) reveals significantly increased plaque deposition in the cerebral cortex of *Psen1*$^{L435F/+}$; *APP*^{MT} mice compared to *Psen1*$^{+/+}$; *APP*^{MT} mice at 9 months of age. Scale bar, 0.25 mm. Data are represented as mean ± SEM. *p < 0.05; **p < 0.01; ***p < 0.001.

See also Figure S3 and Table S2.

ratio is increased; in soluble fractions, levels of human Aβ40 are markedly reduced, and the Aβ42/Aβ40 ratio is increased, although levels of Aβ42 are not significantly changed (Figure 4A). No amyloid plaque deposition was detected in the cerebral cortex of *Psen1*$^{L435F/+}$; *APP*^{WT} mice even at the age of 18 months (Figure S3).

Similarly, we measured levels of human Aβ40 and Aβ42 in insoluble and soluble fractions from the cerebral cortex of *Psen1*$^{L435F/+}$; *APP*^{MT} and *Psen1*$^{+/+}$; *APP*^{MT} mice at 2 months of age (Figure 4B). In *Psen1*$^{L435F/+}$; *APP*^{MT} mice, steady-state levels of human Aβ40 are significantly reduced in insoluble fractions, and the Aβ42/Aβ40 ratio is increased (Figure 4B). Furthermore,

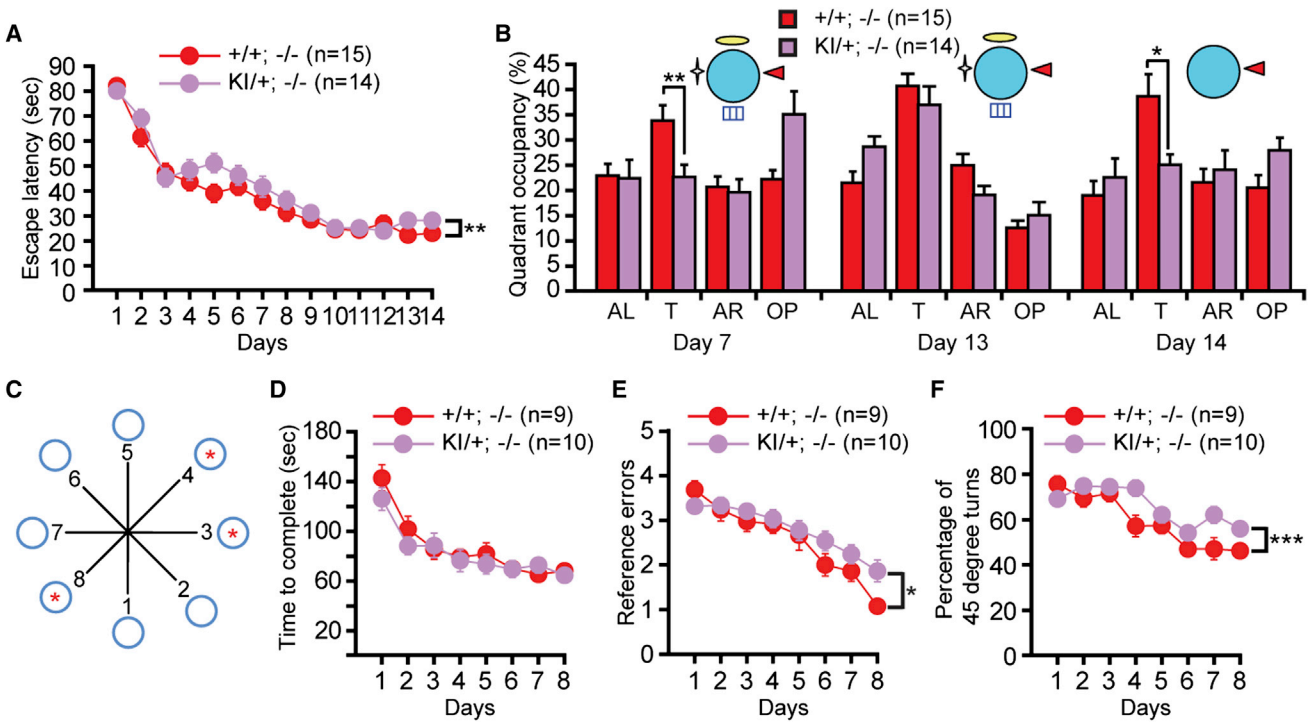

Figure 5. Memory Impairment Caused by the L435F Mutation

(A) *Psen1*$^{L435F/+}$; *Psen2*$^{-/-}$ (KI/+; −/−) mice (n = 14) showed significantly higher escape latencies than *Psen1*$^{+/+}$; *Psen2*$^{-/-}$ (+/+; −/−) littermates (n = 15) during the 14-day training period ($F_{1, 27} = 8.06$; $p < 0.01$) in the Morris water maze test.

(B) *Psen1*$^{L435F/+}$; *Psen2*$^{-/-}$ mice show significantly reduced target quadrant occupancy in the day 7 probe test, but both genotypic groups show similar target quadrant occupancy in the day 13 probe test. *Psen1*$^{L435F/+}$; *Psen2*$^{-/-}$ mice display significantly reduced quadrant occupancy in the partial-cue probe test on day 14. T, target quadrant; AL, adjacent left quadrant; AR, adjacent right quadrant; OP, opposite quadrant.

(C) Naive *Psen1*$^{L435F/+}$; *Psen2*$^{-/-}$ mice (n = 10) and littermate controls (n = 9) were subjected to 8 days of training to locate the three baited arms (indicated by red *) following fasting in the radial arm maze test.

(D) *Psen1*$^{L435F/+}$; *Psen2*$^{-/-}$ and control mice require similar amounts of time to complete the food search ($F_{1, 17} = 1.18$, $p > 0.05$) during the 8-day radial arm maze training.

(E) *Psen1*$^{L435F/+}$; *Psen2*$^{-/-}$ mice display significantly more reference errors ($F_{1, 17} = 4.59$, $p < 0.05$) during the 8-day training period.

(F) *Psen1*$^{L435F/+}$; *Psen2*$^{-/-}$ mice show significantly higher percentages of 45° turns ($F_{1, 17} = 13.63$, $p < 0.001$) during the 8-day training period. Data are represented as mean ± SEM. *$p < 0.05$; **$p < 0.01$; ***$p < 0.001$.

See also Figure S4.

Aβ immunostaining disclosed accelerated amyloid deposition in the cerebral cortex of *Psen1*$^{L435F/+}$; *APP*^{MT} mice compared to *Psen1*$^{+/+}$; *APP*^{MT} mice at 9 months of age (Figure 4C). Thus, although the L435F mutation abolishes the γ-secretase activity of mutant PS1 protein, heterozygosity for the mutation nevertheless enhances the Aβ42/Aβ40 ratio and promotes amyloid deposition.

Memory Impairment Caused by the L435F Mutation

To determine the impact of the L435F mutation on hippocampal learning and memory, we assessed the performance of *Psen1*$^{L435F/+}$; *Psen2*$^{-/-}$ (KI/+; −/−) mice and *Psen1*$^{+/+}$; *Psen2*$^{-/-}$ (+/+; −/−) control littermates using the Morris water maze and radial arm maze tasks. Previous work has shown that PS2 expression is upregulated in the absence of PS1 (Watanabe et al., 2014), which may compensate for behavioral and synaptic deficits caused by PS1 deficiency. We therefore examined the impact of the L435F mutation on behavioral and synaptic phenotypes in a *Psen2*$^{-/-}$ background. We first analyzed hippocampal reference memory in the hidden-platform Morris water maze task. *Psen1*$^{L435F/+}$; *Psen2*$^{-/-}$ mice exhibited significantly higher latencies across the 14-day training period ($p < 0.01$, Figure 5A) and displayed significantly lower target quadrant occupancy in the probe test at day 7 ($p < 0.01$, Figure 5B), indicating impaired reference memory acquisition. Both genotypic groups showed similar target quadrant occupancies in the probe trial at day 13 (Figure 5B), suggesting that additional training overcame this reference memory deficit.

The hippocampus mediates pattern completion during memory recall, an ability to retrieve stored memory traces in response to incomplete sensory cues (Nakazawa et al., 2002). Neuropsychological analysis has shown evidence for impaired behavioral pattern completion in AD patients (Ally et al., 2013). To assess pattern completion, we removed three of the four distal spatial cues and administered another probe trial at day 14. Despite their normal quadrant occupancy under full-cue conditions on day 13, *Psen1*$^{L435F/+}$; *Psen2*$^{-/-}$ mice displayed reduced target quadrant occupancy under partial-cue conditions ($p < 0.05$,

Figure 5B), suggesting impaired hippocampal pattern completion. *Psen1*$^{L435F/+}$; *Psen2*$^{-/-}$ mice exhibited normal escape latency, path length, and swim speed in the visible platform water maze task (Figure S4), indicating that the observed learning and memory impairments are not attributable to deficits in vision, motivation, or sensorimotor abilities.

To obtain an independent assessment of hippocampal memory, we further subjected naive *Psen1*$^{L435F/+}$; *Psen2*$^{-/-}$ and littermate control mice to a spatial discrimination version of the radial arm maze task (Dillon et al., 2008; Rossi-Arnaud et al., 1991). *Psen1*$^{L435F/+}$; *Psen2*$^{-/-}$ and their littermate controls were trained to locate three baited arms over 8 consecutive days (Figure 5C). Although both genotypic groups required similar amounts of time to complete the task (Figure 5D), *Psen1*$^{L435F/+}$; *Psen2*$^{-/-}$ mice showed more reference memory errors ($p < 0.05$, Figure 5E) and a higher proportion of 45° turns into adjacent arms ($p < 0.001$, Figure 5F). Thus, multiple behavioral tasks revealed hippocampal spatial memory deficits caused by the L435F KI mutation.

Synaptic Dysfunction Caused by the L435F Mutation

We then performed electrophysiological analysis on *Psen1*$^{L435F/+}$; *Psen2*$^{-/-}$ mice and *Psen1*$^{+/+}$; *Psen2*$^{-/-}$ littermate controls to determine the effect of the L435F mutation on hippocampal synaptic function and to investigate the cellular mechanism underlying the identified memory defects. Whereas basal synaptic transmission was normal in the Schaffer collateral pathway (Figure 6A), *Psen1*$^{L435F/+}$; *Psen2*$^{-/-}$ mice displayed impaired short-term plasticity, as indicated by reduced paired-pulse facilitation (Figure 6B) and frequency facilitation (Figure 6C). As the impairment in frequency facilitation was already maximal at the 5-Hz stimulation frequency, we tested whether the observed deficits in short-term synaptic plasticity at this frequency of presynaptic activation could affect the inducibility of long-term potentiation (LTP) at the Schaffer collateral-CA1 synapses. Using voltage-clamp recording, we found that LTP induced by pairing presynaptic stimuli with postsynaptic depolarization was significantly reduced in *Psen1*$^{L435F/+}$; *Psen2*$^{-/-}$ mice compared to littermate controls (Figure 6D), whereas NMDAR-mediated EPSCs were unaffected (Figure S5). These impairments resemble the synaptic phenotypes previously identified in mice with conditional *Psen1/2* inactivation (Saura et al., 2004; Zhang et al., 2009, 2010).

We further assessed synaptic plasticity at commissural/associational (C/A)-CA3 synapses, as pattern completion is thought to be mediated by the recurrent collateral connectivity of CA3 neurons (Nakazawa et al., 2002). We found that LTP was impaired at (C/A)-CA3 synapses in *Psen1*$^{L435F/+}$; *Psen2*$^{-/-}$ mice (Figure 6E). Moreover, short-term depression during the initial phase of the LTP-inducing stimulus train was increased at (C/A)-CA3 synapses of *Psen1*$^{L435F/+}$; *Psen2*$^{-/-}$ mice (Figure 6F). These data indicate that the L435F mutation impairs short-term and long-term synaptic plasticity at hippocampal CA1 and CA3 synapses.

The L435F Mutation Causes Age-Dependent Neurodegeneration

Conditional inactivation of PS in the adult cerebral cortex using the *Camk2a-Cre* transgene causes severe, age-dependent neurodegeneration (Saura et al., 2004; Wines-Samuelson et al., 2010). Further analysis of *Psen* conditional knockout mice with varying *Psen2* gene dosage showed that partial inactivation of PS also results in age-dependent neurodegeneration, though with lesser severity and a later age of onset (Watanabe et al., 2014). To examine the impact of the L435F mutation on neuronal survival, relative to the *Psen1* wild-type allele, we generated *Psen1*$^{F/L435F}$; *Psen2*$^{-/-}$; *Camk2a-Cre* mice and littermate *Psen1*$^{F/+}$; *Psen2*$^{-/-}$; *Camk2a-Cre* and *Psen1*$^{F/F}$; *Psen2*$^{-/-}$ mice. Remarkably, *Psen1*$^{F/L435F}$; *Psen2*$^{-/-}$; *Camk2a-Cre* mice display age-dependent neurodegeneration throughout the cerebral cortex, with marked reductions in cortical volume (31.5% ± 5.2%) and neuron number (22.1% ± 1.4%) at 18 months of age (Figure 7A), whereas *Psen1*$^{F/+}$; *Psen2*$^{-/-}$; *Camk2a-Cre* mice, which have one wild-type *Psen1* allele, show no neurodegeneration (Figure 7A). Moreover, increased apoptosis was identified by TUNEL staining (Figure 7B) and cleaved caspase-3 immunostaining (Figure 7C) in the neocortex of *Psen1*$^{F/L435F}$; *Psen2*$^{-/-}$; *Camk2a-Cre* mice.

We further evaluated astrogliosis and microgliosis, as inflammatory responses often accompany neurodegeneration. Immunohistochemical and western analyses reveal enhanced GFAP levels in the cortex of *Psen1*$^{F/L435F}$; *Psen2*$^{-/-}$; *Camk2a-Cre* mice (Figure 7D), indicating the occurrence of astrogliosis in these mice. We also found that immunoreactivity for the microglial marker Iba1 is elevated in the neocortex and hippocampus of *Psen1*$^{F/L435F}$; *Psen2*$^{-/-}$; *Camk2a-Cre* mice (Figure S6), indicating that neurodegeneration is also associated with microgliosis. These data demonstrate that the L435F mutation abolishes the ability of PS1 to support neuronal survival during aging.

DISCUSSION

Large numbers of *PSEN* mutations are linked to FAD, but how these mutations cause the disease remains unresolved. Earlier studies in patient plasma, transgenic mice, and cell lines found that *PSEN* mutations increased Aβ42 levels and/or the Aβ42/Aβ40 ratio (Borchelt et al., 1996; Duff et al., 1996; Hardy and Selkoe, 2002; Scheuner et al., 1996), leading to the hypothesis that *PSEN* mutations cause FAD via a gain-of-function mechanism mediated by selective overproduction of Aβ42 (Hardy and Selkoe, 2002). Interestingly, genetic rescue studies in *C. elegans* showed that *PSEN* mutations resulted in partial loss of PS activity (Levitan et al., 1996). However, overexpression of the *Psen1* A246E transgene rescued the phenotypes of *Psen1*$^{-/-}$ mice (Davis et al., 1998; Qian et al., 1998), and KI mice carrying the *Psen1* M146V mutation did not exhibit phenotypes of *Psen1*$^{-/-}$ mice (Guo et al., 1999), though they exhibited hippocampal memory deficits (Sun et al., 2005). These findings suggested that *PSEN* mutations might not impair PS function in the mammalian brain.

Subsequent genetic studies yielded the surprising discovery that loss of PS function in the adult cerebral cortex recapitulates key features of AD, including progressive memory deficits and age-dependent, widespread neurodegeneration (Beglopoulos et al., 2004; Saura et al., 2004; Wines-Samuelson et al., 2010). Furthermore, similar genetic analysis of another γ-secretase component, Nicastrin, confirmed the importance of γ-secretase

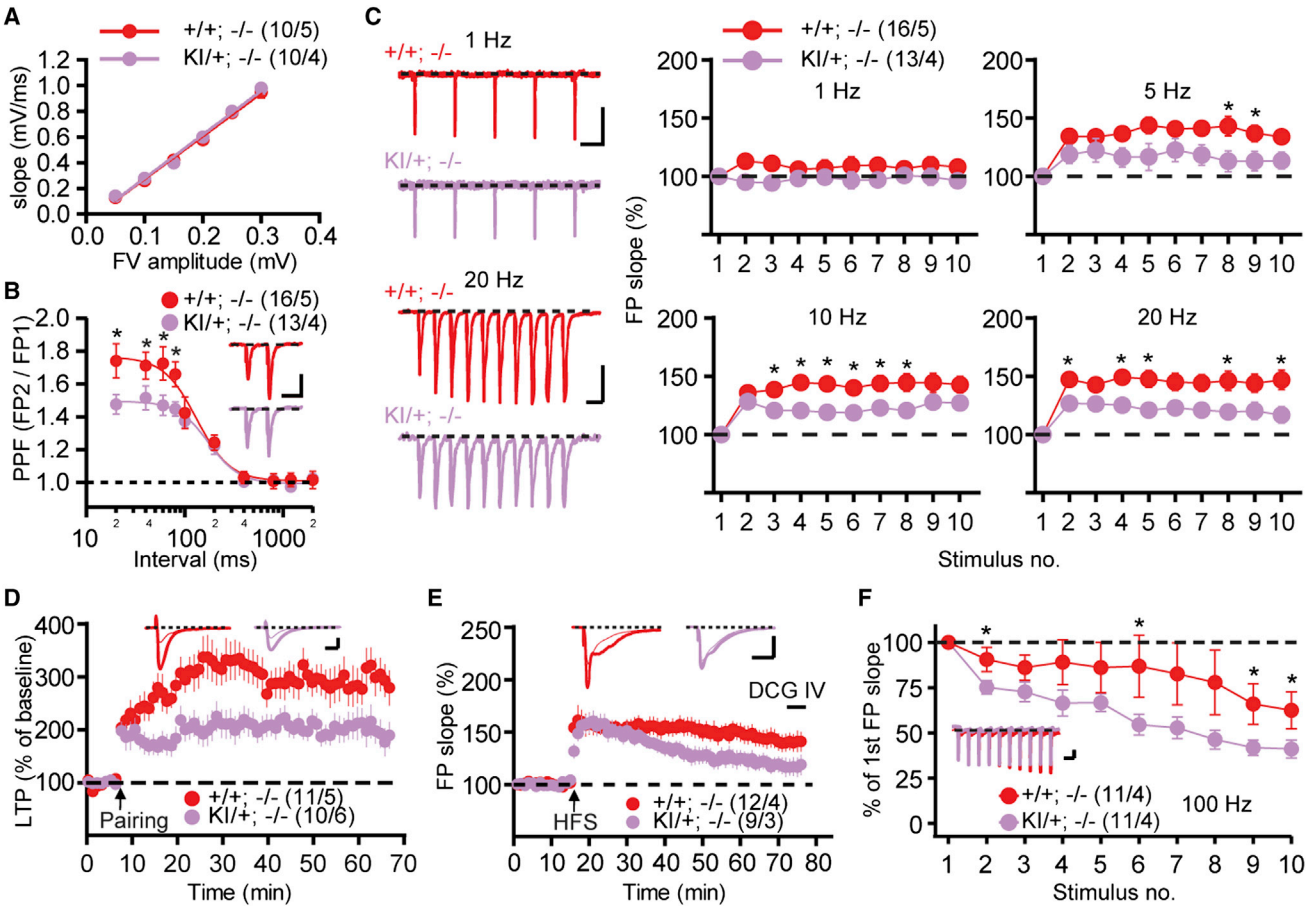

Figure 6. Synaptic Dysfunction Caused by the L435F Mutation

(A) Normal basal synaptic transmission in *Psen1*$^{L435F/+}$; *Psen2*$^{-/-}$ mice. The synaptic input-output relationship was obtained by plotting the fiber volley amplitude against the initial slope of the evoked fEPSP. Each point represents data averaged across all slices for a narrow bin of FV amplitude. The lines represent the best linear regression fit.

(B) Reduced paired-pulse facilitation (PPF) in *Psen1*$^{L435F/+}$; *Psen2*$^{-/-}$ mice. The graph depicts the paired-pulse response ratio obtained at different inter-stimulus intervals (in ms). Scale bar, 1 mV, 50 ms.

(C) Synaptic facilitation elicited by stimulus trains of the indicated frequencies in *Psen1*$^{L435F/+}$; *Psen2*$^{-/-}$ and littermate control mice. Frequency facilitation is significantly decreased in the 5–20 Hz range in *Psen1*$^{L435F/+}$; *Psen2*$^{-/-}$ mice. Scale bar, 1 Hz: 1 mV, 500 ms; 20 Hz: 1 mV, 50 ms. FP, field potential.

(D) Pairing-induced LTP at the Schaffer collateral-CA1 synapses in slices from *Psen1*$^{L435F/+}$; *Psen2*$^{-/-}$ mice and littermate controls. Representative traces before (thin) and after (thick) LTP induction are shown. Insets show the average of 15 EPSCs recorded before and 45–50 min after the induction. Scale bar, 20 ms, 50 pA.

(E) LTP induced at the recurrent commissural/associational (C/A)-CA3 synapses in slices from *Psen1*$^{L435F/+}$; *Psen2*$^{-/-}$ mice and littermate controls. LTP was induced with three trains of high-frequency stimulation (HFS). Representative traces before (thin) and after (thick) LTP induction are shown. Superimposed traces are averages of four consecutive responses 1 min before and 50 min after HFS. The lack of response to DCG IV, which selectively inhibits mossy fiber LTP, confirms that the responses are obtained from (C/A)-CA3 synapses. Scale bar, 10 ms, 0.5 mV.

(F) Increased synaptic depression at (C/A)-CA3 synapses during LTP-inducing stimulation in *Psen1*$^{L435F/+}$; *Psen2*$^{-/-}$ mice. Insets show representative fEPSP traces obtained during single stimulation train. Scale bar, 10 ms, 2 mV.

The values in parentheses indicate the number of neurons or slices (left) and the number of mice (right) used in each experiment. Data are represented as mean ± SEM. *p < 0.05; **p < 0.01; ***p < 0.001.

See also Figure S5.

in memory, synaptic function, and neuronal survival (Lee et al., 2014; Tabuchi et al., 2009). In principle, there are two potential explanations for these unexpected in vivo findings: the essential roles played by PS in the maintenance of memory and synaptic function and protection of cortical neurons from neurodegeneration may represent mere coincidence with no relevance to FAD; or alternatively, pathogenic *PSEN* mutations compromise the essential physiological roles of PS in memory, synaptic function, and neuronal survival, leading over time to neurodegeneration and dementia in FAD.

The current study was designed to address this important unanswered question as to whether *PSEN* mutations indeed compromise the essential functions of PS in the brain, particularly with respect to adult brain phenotypes relevant to FAD. We chose two independent mutations *PSEN1* L435F and C410Y, both of which were clinically and neuropathologically

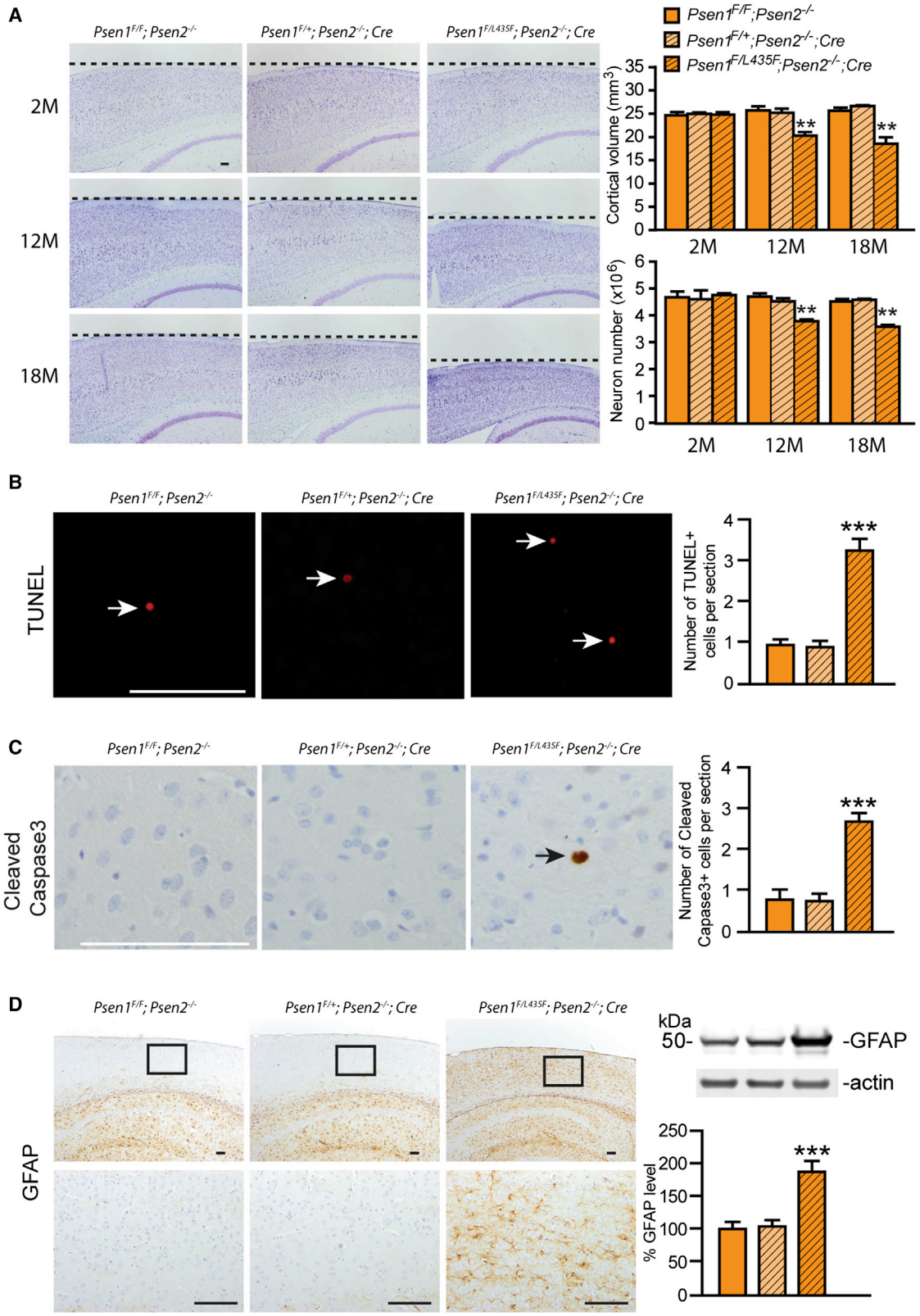

(legend on next page)

confirmed in multiple early-onset FAD families (Campion et al., 1995, 1999; Goudsmit et al., 1981; Heilig et al., 2010; Poorkaj et al., 1998; Rogaeva et al., 2001; Sherrington et al., 1995). Each mutation was introduced into the genomic locus of the *Psen1* gene, so that the FAD mutations are expressed under the control of the endogenous regulatory elements as in human patients. Thus, these KI mice are genetically equivalent to human FAD patients carrying the same *PSEN1* mutation.

To our great surprise, both homozygous L435F and C410Y KI/KI mice are phenotypically indistinguishable from *Psen1*$^{-/-}$ mice (Shen et al., 1997) and exhibit perinatal lethality with complete penetrance (Figure 1, Table S1). However, in contrast to the absence of *Psen1* mRNA and protein in *Psen1*$^{-/-}$ mice, levels of *Psen1* mRNA are normal in the brain of L435F and C410Y KI/KI mice (Figure 1). Levels of PS1 NTFs and CTFs are drastically reduced in the brain of L435F and C410Y KI/KI mice with a greater reduction by the L435F mutation (Figure 1). This minor difference between the two mutations correlates with the severity of the phenotypes in L435F and C410Y KI/KI newborn pups (Figure 1) and is consistent with earlier reports regarding the functional impairment of the presenilinase and γ-secretase activity caused by these two mutations (Heilig et al., 2010, 2013). Corresponding to these changes, PS1 holoprotein accumulates in the L435F and C410Y KI/+ and KI/KI brains in a KI allele dosage-dependent manner (Figure 1). Importantly, PS1 holoprotein appears to participate in the stable γ-secretase complex, as levels of other γ-secretase components are unaffected in KI/KI mice but are reduced in *Psen1*$^{-/-}$ mice (Figure S1). Thus, the L435F and C410Y mutations do not affect *Psen1* mRNA expression, but drastically reduce presenilinase activity and the production of the functional PS1 NTFs and CTFs.

Further analysis revealed impaired neurogenesis and reduced neural progenitor population in L435F and C410Y KI/KI brains (Figure 2), similar to *Psen1* null embryos (Handler et al., 2000; Shen et al., 1997). Notch signaling evaluated by the expression of the Notch target *Hes5* is reduced in L435F and C410Y KI/KI embryonic brains (Figure 2). NICD production, measured by an in vitro γ-secretase assay, is reduced in L435F and C410Y KI/+ brains and abolished in L435F and C410Y KI/KI brains (Figure 2), indicating that both L435F and C410Y mutations eliminate γ-secretase activity. This interpretation is further supported by the findings that the CTFs of APP and N-cadherin, both of which are γ-secretase substrates, accumulate dramatically in L435F and C410Y KI/KI brains to a level comparable to that of *Psen1*$^{-/-}$ brains (Figure 3, Figure S2) and that γ-secretase-mediated production of Aβ40 and Aβ42 is abolished in KI/KI brains (Figure 3). These data demonstrate that the L435F and C410Y mutations abolish γ-secretase activity, leading to accumulation of γ-secretase substrates and impairment of Notch signaling and neurogenesis. This study demonstrates that FAD mutations in the *PSEN* genes can cause complete loss of its function and γ-secretase activity in vivo and can recapitulate *Psen1* null phenotypes in homozygosity.

The loss of PS1 and γ-secretase function brought about in vivo by the L435F and C410Y mutations is remarkably consistent with their previously reported effects in a sensitive cell-based system (Heilig et al., 2010, 2013). These mutations are likely particularly deleterious to γ-secretase activity due to their predicted proximity to the enzyme active site (Sato et al., 2008) and the introduction of bulky aromatic side chains, which likely disrupts the structure of γ-secretase. Analysis of a panel of FAD mutations in the same cell-based system demonstrated uniform impairment of γ-secretase activity, with the severity varying among mutations (Heilig et al., 2010, 2013). Thus, we suggest that the loss of in vivo function conferred by the L435F and C410Y mutations analyzed here represents a general property of FAD mutations. Our findings may differ from previously reported *PSEN1* KI (e.g., M146V) and transgenic mice due to the varying severity of different *PSEN1* mutations on impairment of γ-secretase activity and due to overexpression of mutant PS1 transgene that could compensate for the partial loss of PS1 function.

In contrast to abolished production of Aβ40 and Aβ42 in KI/KI embryonic brains, their production is reduced in KI/+ embryonic and adult brains measured by in vitro γ-secretase assay (Figure 3). Steady-state levels of Aβ40 and Aβ42 measured by ELISA are also reduced in the KI/+ adult brain, and the reduction of Aβ40 is slightly greater than that of Aβ42, leading to a modest, but significant, increase (~15%) of the Aβ42/Aβ40 ratio (Figure 3). Similar results (Figure 4, Table S2) were obtained when L435F KI/+ mice were crossed to *APP* transgenic mice overexpressing (~2-fold) either human wild-type (I5 line) or mutant (J20 line) APP containing both the Swedish and the Indiana mutations (Mucke et al., 2000). Strikingly, heterozygosity for the L435F KI mutation markedly accelerates amyloid deposition in mutant *APP* transgenic mice (Figure 4). This finding demonstrates that *PSEN* mutations can act through a loss-of-function mechanism to elevate the Aβ42/Aβ40 ratio and thereby promote amyloid deposition. Since production of Aβ40 and Aβ42 measured by in vitro

Figure 7. The L435F Mutation Causes Age-Dependent Neurodegeneration

(A) Comparison of brain morphology between *Psen1*$^{F/L435F}$; *Psen2*$^{-/-}$; *Cre* mice and littermate controls at 2, 12, and 18 months of age. Left: images of Nissl-stained comparable sagittal brain sections. Right: cortical volume and neuron number obtained by stereological quantification following Nissl staining and NeuN immnostaining, respectively. Cortical volume and neuron number are normal at 2 months of age but significantly reduced at 12 (~22%) and 18 (~32%) months of age in *Psen1*$^{F/L435F}$; *Psen2*$^{-/-}$; *Cre* mice relative to controls (n ≥ 3 for each genotype at each age). Scale bar, 0.1 mm.

(B) More TUNEL-positive cells are observed in the cerebral cortex of *Psen1*$^{F/L435F}$; *Psen2*$^{-/-}$; *Cre* mice (n = 3) compared to control mice (n = 4) at 18 months of age. Scale bar, 0.1 mm.

(C) More active caspase-3-positive cells are detected in the cerebral cortex of *Psen1*$^{F/L435F}$; *Psen2*$^{-/-}$; *Cre* mice (n = 3) relative to control mice (n = 4) at 18 months of age. Scale bar, 0.1 mm.

(D) Increased GFAP immunoreactivity in the cortex of *Psen1*$^{F/L435F}$; *Psen2*$^{-/-}$; *Cre* mice at 12 months of age indicates astrogliosis. Bottom images show higher-magnification views of the boxed area in the cortex. Western analysis also shows increased levels of GFAP in the cortex of *Psen1*$^{F/L435F}$; *Psen2*$^{-/-}$; *Cre* mice (KI) compared to littermate control *Psen1*$^{F/F}$; *Psen2*$^{-/-}$ and *Psen1*$^{F/+}$; *Psen2*$^{-/-}$; *Cre* mice (n = 8 for each genotype). Data are represented as mean ± SEM. *p < 0.05; **p < 0.01; ***p < 0.001. Scale bar, 0.1 mm.

See also Figure S6.

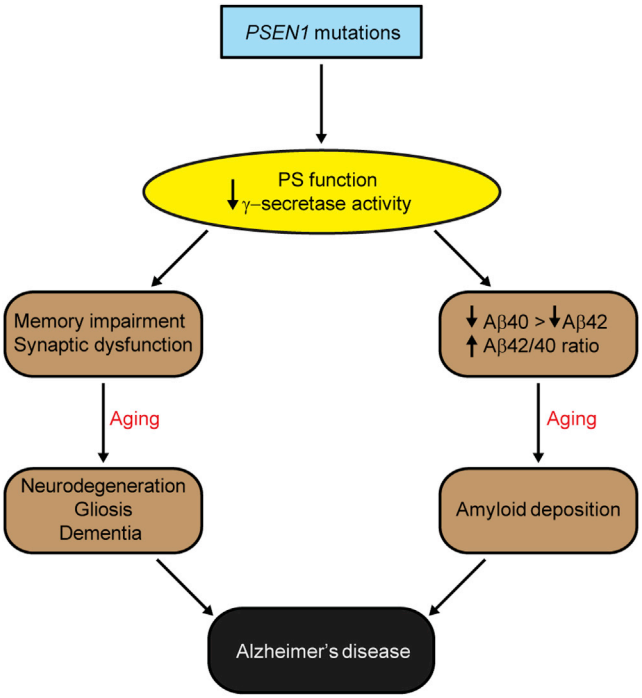

Figure 8. A Schematic Model for FAD

Pathogenic *PSEN1* mutations cause loss of PS1 function and γ-secretase activity, leading to AD-relevant functional and neuropathological changes, including memory impairment, synaptic dysfunction, age-dependent neurodegeneration, gliosis, and dementia. In parallel, the loss of PS function produced by pathogenic *PSEN1* mutations also reduces Aβ production and increases the Aβ42/Aβ40 ratio due to the greater reduction of Aβ40 production compared to that of Aβ42, thereby promoting amyloid plaque deposition. Thus, *PSEN* mutations produce the full spectrum of AD phenotypes through a loss-of-function mechanism.

γ-secretase assay is reduced to comparable extents by the heterozygous L435F KI mutation (Figure 3), the greater reduction in steady-state accumulation of Aβ40 relative to Aβ42 may reflect their differential clearance.

Synaptic dysfunction is thought to be a pathogenic precursor of frank neurodegeneration, and the hippocampus is particularly vulnerable in AD. Relative to wild-type PS1, the L435F mutation leads to impaired short-term synaptic plasticity and LTP in the hippocampal Schaffer collateral pathway (Figure 6; Figure S5). These synaptic deficits are compatible with the spatial memory deficits observed in the hidden platform version of the water maze, the radial arm maze, and the pattern completion tasks (Figure 5; Figure S4). Similar synaptic and memory deficits were also observed in *Psen* conditional knockout mice (Saura et al., 2004; Zhang et al., 2009, 2010). Consistent with the pattern completion deficits observed in the KI mice (Figure 5), LTP is also impaired in the commissural/associational pathway in hippocampal area CA3, which is thought to play a crucial role in this process (Figure 6; Figure S5). The pattern completion deficit exhibited by L435F KI mice parallels the impaired behavioral pattern completion reported in AD patients (Ally et al., 2013).

Importantly, compared to the wild-type *Psen1* allele, the L435F mutant allele is incapable of supporting normal neuronal survival and preventing neurodegeneration in the aging brain and causes age-dependent neurodegeneration, as shown by progressive loss of cortical neurons and increases of apoptosis as well as astrogliosis and microgliosis (Figure 7; Figure S6). Thus, this study provides an animal model in which a pathogenic FAD mutation causes progressive and widespread neurodegeneration. Our findings are consistent with prior reports indicating that *PSEN* mutations could enhance apoptosis in cultured cells (Vito et al., 1996; Wolozin et al., 1996). Interestingly, the extent of neurodegeneration associated with the *Psen1* L435F mutation is less severe compared to that in *Psen* conditional knockout mice, raising the possibility that PS1 holoprotein may partially support neuronal survival in the aging brain despite its essentially complete loss of γ-secretase activity. Further studies will be needed to elucidate the underlying mechanism.

More than 80% of identified FAD mutations reside within the *PSEN* genes, but the pathogenic mechanism remains unresolved. While earlier studies supported a toxic gain-of-function pathogenic mechanism based on excessive production of Aβ42 (Borchelt et al., 1996; Duff et al., 1996; Scheuner et al., 1996), this hypothesis is at odds with several lines of experimental data. For example, overproduction of Aβ42, even at massive levels (e.g., J20 mice overproduce Aβ42 >40-fold at 2 months and >6,400-fold at 17 months), did not produce significant neurodegeneration in mouse models (Irizarry et al., 1997; Saura et al., 2005). Human FAD patients carrying *PSEN1* mutations develop the disease at earlier ages than APP mutation carriers (Ryman et al., 2014), even though *PSEN1* mutations have modest effects on the Aβ42/Aβ40 ratio in mice (e.g., ~15% increase for the L435F mutation while overall production of Aβ42 and Aβ40 is reduced). Furthermore, FAD *PSEN* mutations cause loss of PS activity in *C. elegans* (Levitan et al., 1996) and in cultured cells (Heilig et al., 2010, 2013; Song et al., 1999), and loss of PS in the adult mouse brain recapitulates widespread age-dependent neurodegeneration, gliosis, memory loss, and synaptic dysfunction (Beglopoulos et al., 2004; Saura et al., 2004; Wines-Samuelson et al., 2010). These observations suggest that the pathogenic mechanism underlying *PSEN* mutations is more complex than initially anticipated. Our in vivo analysis of two independent clinical *PSEN1* mutations provides important experimental support for the Presenilin hypothesis, which posits that loss of PS function plays an important role in the pathogenesis of FAD (Kelleher and Shen, 2010; Shen and Kelleher, 2007).

Through the development and multidisciplinary analysis of KI mice expressing *PSEN1* mutations, the current study reveals two parallel pathways affected by *PSEN* mutations that are relevant to FAD pathogenesis (Figure 8). Pathogenic *PSEN* mutations cause synaptic dysfunction, memory impairment, and age-dependent neurodegeneration via a loss of essential PS functions. In addition, loss of PS function conferred by *PSEN* mutations promotes amyloid pathology by inhibiting γ-secretase activity, decreasing Aβ production, and increasing the Aβ42/40 ratio due to a greater relative reduction in Aβ40 accumulation (Figure 8). An intriguing implication of our findings is that therapeutic strategies aimed at restoring, rather than inhibiting, normal PS function in the brain may hold promise for the effective treatment of AD.

EXPERIMENTAL PROCEDURES

A brief description of the experimental procedures is included below, and full experimental details can be found in the Supplemental Information.

Generation of *Psen1* L435F and C410Y KI Mice

Targeting vectors for the generation of the L435F and C410Y KI alleles were constructed by PCR amplification of the 5′ and 3′ homologous sequences from genomic DNA followed by site-directed mutagenesis to introduce the mutation (1303C→T in exon 12 for L435F, 1229G→A in exon 11 for C410Y). The targeting vector was transfected into embryonic stem cells (ESCs), and the ESCs carrying the correct homologous recombination events were screened and confirmed by Southern analysis. The correctly targeted ESCs were injected into blastocysts to generate chimeric mice. Mice carrying the targeted allele were crossed with *Camk2a-Cre* transgenic mice (Saura et al., 2004) to remove the floxed *neomycin* cassette and produce heterozygous KI mice. L435F KI/+ mice were crossed with $Psen2^{-/-}$ (Steiner et al., 1999) to generate $Psen1^{L435F/+}$; $Psen2^{-/-}$ mice, which were further crossed with $Psen1^{F/F}$; $Psen2^{-/-}$; *Camk2a-Cre* mice to generate $Psen1^{F/L435F}$; $Psen2^{-/-}$; *Camk2a-Cre* mice. Mice were maintained on the C57BL6/J-129 hybrid genetic background, and littermate controls were used for all analysis. Electrophysiological, behavioral, histological, and biochemical analyses were performed in a genotype-blind manner. All procedures relating to animal care and treatment conformed to institutional and NIH guidelines.

In Vitro γ-Secretase Assay

γ-Secretase activities were measured by cell-free in vitro assay using CHAPSO-solubilized brain fractions and bacterially expressed recombinant proteins as substrates (Takahashi et al., 2003). See Supplemental Information for full experimental details.

ELISA

Aβ40 and Aβ42 generated in in vitro assays were measured using the 11A50-B10/4G8 and 12F4/4G8 sandwich ELISA, respectively (Watanabe et al., 2012), and the Aβ antibodies were purchased from Covance. Endogenous mouse and human Aβ40 and Aβ42 were measured by MSD 96-well MULTI-SPOT Human/Rodent (4G8) Abeta Triplex Ultra-sensitive Assay (MesoScale Discovery). See Supplemental Information for full experimental details.

Behavioral Analysis

Littermate male mice were used in the behavioral tests. For the Morris water maze tasks, mice were trained for 14 days with four trials daily, and the full-cue probe tests were administered at days 7 and 13, and the partial-cue probe test was administered at day 14. For the radial arm maze, all mice were single housed and fed restrictively to reduce and maintain their body weight by 20% before and during the 8-day training session. See Supplemental Information for full experimental details.

Electrophysiological Analysis

Acute hippocampal slices (400 μm) were prepared and recorded as described previously (Zhang et al., 2009). See Supplemental Information for full experimental details of field and whole-cell recording at hippocampal Schaffer collateral-CA1 synapses and recurrent commissural/associational-CA3 synapses.

Histological Analysis

Embryonic brains were dissected at E16.5 and processed for serial paraffin sections (10 μm). Every fifth section was stained with H&E, and comparable sections from both genotypic groups were compared. The number of Ki67-immunoreactive cells was quantified using four comparable sections per brain and four brains per genotype. Adult brains were perfused with PBS, fixed in 4% PFA, processed for paraffin embedding, and serially sectioned (10 μm). Adult brain sections were stained with 0.5% cresyl violet (Nissl) or immunostained with antibodies against NeuN (1:300; Millipore), cleaved caspase-3 (1:100; Cell Signaling Technology), GFAP (1:500; Sigma), Iba1 (1:250; Wako), and Aβ (R1282; 1:1,000).

Statistical Analysis

Statistical analysis was performed using one-way ANOVA or two-tailed unpaired Student's t test for all comparisons of the biochemical, behavioral, and electrophysiological results, except that two-way ANOVA was used to determine the genotypic effects on latencies in the water maze, reference errors and percentages of 45° turns in the radial arm maze, and EPSCs of NMDAR. A value of $p < 0.05$ was considered significant. All data are represented as mean ± SEM.

SUPPLEMENTAL INFORMATION

Supplemental Information includes Supplemental Experimental Procedures, six figures, and two tables and can be found with this article online at http://dx.doi.org/10.1016/j.neuron.2015.02.010.

AUTHOR CONTRIBUTIONS

J.S. and R.J.K. conceived and directed the project; D.X., J.S., and R.J.K. designed experiments and analyzed data; D.X. performed most experiments and generated figures; H.W., B.W., S.H.L., Y.L., E.T., and V.Y.B. performed experiments and contributed to figures; and D.X., J.S., and R.J.K wrote the paper.

ACKNOWLEDGMENTS

We would like to thank T. Südhof for critical reading of the manuscript, L. Mucke for APP transgenic mice, T. Iwatsubo and T. Tomita for the pTrcHis2A-C100-FmH and pTrcHis2A-N102-FmH plasmids, E. Heilig, T. Ding, and H. Zhao for assistance, and other lab members for helpful discussions. This work was supported by grants from the NIH (R01NS041783 and R01NS042818 to J.S., R01NS075346 to R.J.K.) and the Alzheimer's Association. R.J.K. was supported by the Pew Scholars Program in the Biomedical Sciences.

Received: November 7, 2014
Revised: December 30, 2014
Accepted: February 4, 2015
Published: March 4, 2015

REFERENCES

Ally, B.A., Hussey, E.P., Ko, P.C., and Molitor, R.J. (2013). Pattern separation and pattern completion in Alzheimer's disease: evidence of rapid forgetting in amnestic mild cognitive impairment. Hippocampus *23*, 1246–1258.

Beglopoulos, V., Sun, X., Saura, C.A., Lemere, C.A., Kim, R.D., and Shen, J. (2004). Reduced beta-amyloid production and increased inflammatory responses in presenilin conditional knock-out mice. J. Biol. Chem. *279*, 46907–46914.

Borchelt, D.R., Thinakaran, G., Eckman, C.B., Lee, M.K., Davenport, F., Ratovitsky, T., Prada, C.M., Kim, G., Seekins, S., Yager, D., et al. (1996). Familial Alzheimer's disease-linked presenilin 1 variants elevate Abeta1-42/1-40 ratio in vitro and in vivo. Neuron *17*, 1005–1013.

Campion, D., Flaman, J.M., Brice, A., Hannequin, D., Dubois, B., Martin, C., Moreau, V., Charbonnier, F., Didierjean, O., Tardieu, S., et al. (1995). Mutations of the presenilin I gene in families with early-onset Alzheimer's disease. Hum. Mol. Genet. *4*, 2373–2377.

Campion, D., Dumanchin, C., Hannequin, D., Dubois, B., Belliard, S., Puel, M., Thomas-Anterion, C., Michon, A., Martin, C., Charbonnier, F., et al. (1999). Early-onset autosomal dominant Alzheimer disease: prevalence, genetic heterogeneity, and mutation spectrum. Am. J. Hum. Genet. *65*, 664–670.

Davis, J.A., Naruse, S., Chen, H., Eckman, C., Younkin, S., Price, D.L., Borchelt, D.R., Sisodia, S.S., and Wong, P.C. (1998). An Alzheimer's disease-linked PS1 variant rescues the developmental abnormalities of PS1-deficient embryos. Neuron *20*, 603–609.

De Strooper, B., Annaert, W., Cupers, P., Saftig, P., Craessaerts, K., Mumm, J.S., Schroeter, E.H., Schrijvers, V., Wolfe, M.S., Ray, W.J., et al. (1999). A

presenilin-1-dependent gamma-secretase-like protease mediates release of Notch intracellular domain. Nature *398*, 518–522.

Dillon, G.M., Qu, X., Marcus, J.N., and Dodart, J.C. (2008). Excitotoxic lesions restricted to the dorsal CA1 field of the hippocampus impair spatial memory and extinction learning in C57BL/6 mice. Neurobiol. Learn. Mem. *90*, 426–433.

Duff, K., Eckman, C., Zehr, C., Yu, X., Prada, C.M., Perez-tur, J., Hutton, M., Buee, L., Harigaya, Y., Yager, D., et al. (1996). Increased amyloid-beta42(43) in brains of mice expressing mutant presenilin 1. Nature *383*, 710–713.

Games, D., Adams, D., Alessandrini, R., Barbour, R., Berthelette, P., Blackwell, C., Carr, T., Clemens, J., Donaldson, T., Gillespie, F., et al. (1995). Alzheimer-type neuropathology in transgenic mice overexpressing V717F beta-amyloid precursor protein. Nature *373*, 523–527.

Goudsmit, J., White, B.J., Weitkamp, L.R., Keats, B.J., Morrow, C.H., and Gajdusek, D.C. (1981). Familial Alzheimer's disease in two kindreds of the same geographic and ethnic origin. A clinical and genetic study. J. Neurol. Sci. *49*, 79–89.

Guo, Q., Fu, W., Sopher, B.L., Miller, M.W., Ware, C.B., Martin, G.M., and Mattson, M.P. (1999). Increased vulnerability of hippocampal neurons to excitotoxic necrosis in presenilin-1 mutant knock-in mice. Nat. Med. *5*, 101–106.

Haleem, K., Lippa, C.F., Smith, T.W., Kowa, H., Wu, J., and Iwatsubo, T. (2007). Presenilin-1 C410Y Alzheimer disease plaques contain synaptic proteins. Am. J. Alzheimers Dis. Other Demen. *22*, 137–144.

Handler, M., Yang, X., and Shen, J. (2000). Presenilin-1 regulates neuronal differentiation during neurogenesis. Development *127*, 2593–2606.

Hardy, J., and Selkoe, D.J. (2002). The amyloid hypothesis of Alzheimer's disease: progress and problems on the road to therapeutics. Science *297*, 353–356.

Heilig, E.A., Xia, W., Shen, J., and Kelleher, R.J., 3rd. (2010). A presenilin-1 mutation identified in familial Alzheimer disease with cotton wool plaques causes a nearly complete loss of gamma-secretase activity. J. Biol. Chem. *285*, 22350–22359.

Heilig, E.A., Gutti, U., Tai, T., Shen, J., and Kelleher, R.J., 3rd. (2013). Trans-dominant negative effects of pathogenic PSEN1 mutations on γ-secretase activity and Aβ production. J. Neurosci. *33*, 11606–11617.

Hsiao, K., Chapman, P., Nilsen, S., Eckman, C., Harigaya, Y., Younkin, S., Yang, F., and Cole, G. (1996). Correlative memory deficits, Abeta elevation, and amyloid plaques in transgenic mice. Science *274*, 99–102.

Irizarry, M.C., McNamara, M., Fedorchak, K., Hsiao, K., and Hyman, B.T. (1997). APPSw transgenic mice develop age-related A beta deposits and neuropil abnormalities, but no neuronal loss in CA1. J. Neuropathol. Exp. Neurol. *56*, 965–973.

Kelleher, R.J., 3rd, and Shen, J. (2010). Genetics. Gamma-secretase and human disease. Science *330*, 1055–1056.

Kim, W.Y., and Shen, J. (2008). Presenilins are required for maintenance of neural stem cells in the developing brain. Mol. Neurodegener. *3*, 2.

Klunk, W.E., Price, J.C., Mathis, C.A., Tsopelas, N.D., Lopresti, B.J., Ziolko, S.K., Bi, W., Hoge, J.A., Cohen, A.D., Ikonomovic, M.D., et al. (2007). Amyloid deposition begins in the striatum of presenilin-1 mutation carriers from two unrelated pedigrees. J. Neurosci. *27*, 6174–6184.

Lee, S.H., Sharma, M., Südhof, T.C., and Shen, J. (2014). Synaptic function of nicastrin in hippocampal neurons. Proc. Natl. Acad. Sci. USA *111*, 8973–8978.

Levitan, D., Doyle, T.G., Brousseau, D., Lee, M.K., Thinakaran, G., Slunt, H.H., Sisodia, S.S., and Greenwald, I. (1996). Assessment of normal and mutant human presenilin function in Caenorhabditis elegans. Proc. Natl. Acad. Sci. USA *93*, 14940–14944.

Li, Y.M., Xu, M., Lai, M.T., Huang, Q., Castro, J.L., DiMuzio-Mower, J., Harrison, T., Lellis, C., Nadin, A., Neduvelil, J.G., et al. (2000). Photoactivated gamma-secretase inhibitors directed to the active site covalently label presenilin 1. Nature *405*, 689–694.

Marambaud, P., Wen, P.H., Dutt, A., Shioi, J., Takashima, A., Siman, R., and Robakis, N.K. (2003). A CBP binding transcriptional repressor produced by the PS1/epsilon-cleavage of N-cadherin is inhibited by PS1 FAD mutations. Cell *114*, 635–645.

Moonis, M., Swearer, J.M., Dayaw, M.P., St George-Hyslop, P., Rogaeva, E., Kawarai, T., and Pollen, D.A. (2005). Familial Alzheimer disease: decreases in CSF Abeta42 levels precede cognitive decline. Neurology *65*, 323–325.

Mucke, L., Masliah, E., Yu, G.Q., Mallory, M., Rockenstein, E.M., Tatsuno, G., Hu, K., Kholodenko, D., Johnson-Wood, K., and McConlogue, L. (2000). High-level neuronal expression of abeta 1-42 in wild-type human amyloid protein precursor transgenic mice: synaptotoxicity without plaque formation. J. Neurosci. *20*, 4050–4058.

Nakazawa, K., Quirk, M.C., Chitwood, R.A., Watanabe, M., Yeckel, M.F., Sun, L.D., Kato, A., Carr, C.A., Johnston, D., Wilson, M.A., and Tonegawa, S. (2002). Requirement for hippocampal CA3 NMDA receptors in associative memory recall. Science *297*, 211–218.

Poorkaj, P., Sharma, V., Anderson, L., Nemens, E., Alonso, M.E., Orr, H., White, J., Heston, L., Bird, T.D., and Schellenberg, G.D. (1998). Missense mutations in the chromosome 14 familial Alzheimer's disease presenilin 1 gene. Hum. Mutat. *11*, 216–221.

Qian, S., Jiang, P., Guan, X.M., Singh, G., Trumbauer, M.E., Yu, H., Chen, H.Y., Van de Ploeg, L.H., and Zheng, H. (1998). Mutant human presenilin 1 protects presenilin 1 null mouse against embryonic lethality and elevates Abeta1-42/43 expression. Neuron *20*, 611–617.

Rogaeva, E.A., Fafel, K.C., Song, Y.Q., Medeiros, H., Sato, C., Liang, Y., Richard, E., Rogaev, E.I., Frommelt, P., Sadovnick, A.D., et al. (2001). Screening for PS1 mutations in a referral-based series of AD cases: 21 novel mutations. Neurology *57*, 621–625.

Rossi-Arnaud, C., Fagioli, S., and Ammassari-Teule, M. (1991). Spatial learning in two inbred strains of mice: genotype-dependent effect of amygdaloid and hippocampal lesions. Behav. Brain Res. *45*, 9–16.

Ryman, D.C., Acosta-Baena, N., Aisen, P.S., Bird, T., Danek, A., Fox, N.C., Goate, A., Frommelt, P., Ghetti, B., Langbaum, J.B., et al.; Dominantly Inherited Alzheimer Network (2014). Symptom onset in autosomal dominant Alzheimer disease: a systematic review and meta-analysis. Neurology *83*, 253–260.

Sato, C., Takagi, S., Tomita, T., and Iwatsubo, T. (2008). The C-terminal PAL motif and transmembrane domain 9 of presenilin 1 are involved in the formation of the catalytic pore of the gamma-secretase. J. Neurosci. *28*, 6264–6271.

Saura, C.A., Choi, S.Y., Beglopoulos, V., Malkani, S., Zhang, D., Shankaranarayana Rao, B.S., Chattarji, S., Kelleher, R.J., 3rd, Kandel, E.R., Duff, K., et al. (2004). Loss of presenilin function causes impairments of memory and synaptic plasticity followed by age-dependent neurodegeneration. Neuron *42*, 23–36.

Saura, C.A., Chen, G., Malkani, S., Choi, S.Y., Takahashi, R.H., Zhang, D., Gouras, G.K., Kirkwood, A., Morris, R.G., and Shen, J. (2005). Conditional inactivation of presenilin 1 prevents amyloid accumulation and temporarily rescues contextual and spatial working memory impairments in amyloid precursor protein transgenic mice. J. Neurosci. *25*, 6755–6764.

Scheuner, D., Eckman, C., Jensen, M., Song, X., Citron, M., Suzuki, N., Bird, T.D., Hardy, J., Hutton, M., Kukull, W., et al. (1996). Secreted amyloid beta-protein similar to that in the senile plaques of Alzheimer's disease is increased in vivo by the presenilin 1 and 2 and APP mutations linked to familial Alzheimer's disease. Nat. Med. *2*, 864–870.

Shen, J., and Kelleher, R.J., 3rd. (2007). The presenilin hypothesis of Alzheimer's disease: evidence for a loss-of-function pathogenic mechanism. Proc. Natl. Acad. Sci. USA *104*, 403–409.

Shen, J., Bronson, R.T., Chen, D.F., Xia, W., Selkoe, D.J., and Tonegawa, S. (1997). Skeletal and CNS defects in Presenilin-1-deficient mice. Cell *89*, 629–639.

Sherrington, R., Rogaev, E.I., Liang, Y., Rogaeva, E.A., Levesque, G., Ikeda, M., Chi, H., Lin, C., Li, G., Holman, K., et al. (1995). Cloning of a gene bearing missense mutations in early-onset familial Alzheimer's disease. Nature *375*, 754–760.

Song, W., Nadeau, P., Yuan, M., Yang, X., Shen, J., and Yankner, B.A. (1999). Proteolytic release and nuclear translocation of Notch-1 are induced by

presenilin-1 and impaired by pathogenic presenilin-1 mutations. Proc. Natl. Acad. Sci. USA *96*, 6959–6963.

Steiner, H., Duff, K., Capell, A., Romig, H., Grim, M.G., Lincoln, S., Hardy, J., Yu, X., Picciano, M., Fechteler, K., et al. (1999). A loss of function mutation of presenilin-2 interferes with amyloid beta-peptide production and notch signaling. J. Biol. Chem. *274*, 28669–28673.

Struhl, G., and Greenwald, I. (1999). Presenilin is required for activity and nuclear access of Notch in Drosophila. Nature *398*, 522–525.

Sun, X., Beglopoulos, V., Mattson, M.P., and Shen, J. (2005). Hippocampal spatial memory impairments caused by the familial Alzheimer's disease-linked presenilin 1 M146V mutation. Neurodegener. Dis. *2*, 6–15.

Tabuchi, K., Chen, G., Südhof, T.C., and Shen, J. (2009). Conditional forebrain inactivation of nicastrin causes progressive memory impairment and age-related neurodegeneration. J. Neurosci. *29*, 7290–7301.

Takahashi, Y., Hayashi, I., Tominari, Y., Rikimaru, K., Morohashi, Y., Kan, T., Natsugari, H., Fukuyama, T., Tomita, T., and Iwatsubo, T. (2003). Sulindac sulfide is a noncompetitive gamma-secretase inhibitor that preferentially reduces Abeta 42 generation. J. Biol. Chem. *278*, 18664–18670.

Vito, P., Lacanà, E., and D'Adamio, L. (1996). Interfering with apoptosis: Ca(2+)-binding protein ALG-2 and Alzheimer's disease gene ALG-3. Science *271*, 521–525.

Watanabe, H., Xia, D., Kanekiyo, T., Kelleher, R.J., 3rd, and Shen, J. (2012). Familial frontotemporal dementia-associated presenilin-1 c.548G>T mutation causes decreased mRNA expression and reduced presenilin function in knock-in mice. J. Neurosci. *32*, 5085–5096.

Watanabe, H., Iqbal, M., Zheng, J., Wines-Samuelson, M., and Shen, J. (2014). Partial loss of presenilin impairs age-dependent neuronal survival in the cerebral cortex. J. Neurosci. *34*, 15912–15922.

Wines-Samuelson, M., Schulte, E.C., Smith, M.J., Aoki, C., Liu, X., Kelleher, R.J., 3rd, and Shen, J. (2010). Characterization of age-dependent and progressive cortical neuronal degeneration in presenilin conditional mutant mice. PLoS ONE *5*, e10195.

Wolozin, B., Iwasaki, K., Vito, P., Ganjei, J.K., Lacanà, E., Sunderland, T., Zhao, B., Kusiak, J.W., Wasco, W., and D'Adamio, L. (1996). Participation of presenilin 2 in apoptosis: enhanced basal activity conferred by an Alzheimer mutation. Science *274*, 1710–1713.

Yu, H., Saura, C.A., Choi, S.Y., Sun, L.D., Yang, X., Handler, M., Kawarabayashi, T., Younkin, L., Fedeles, B., Wilson, M.A., et al. (2001). APP processing and synaptic plasticity in presenilin-1 conditional knockout mice. Neuron *31*, 713–726.

Zhang, C., Wu, B., Beglopoulos, V., Wines-Samuelson, M., Zhang, D., Dragatsis, I., Südhof, T.C., and Shen, J. (2009). Presenilins are essential for regulating neurotransmitter release. Nature *460*, 632–636.

Zhang, D., Zhang, C., Ho, A., Kirkwood, A., Südhof, T.C., and Shen, J. (2010). Inactivation of presenilins causes pre-synaptic impairment prior to post-synaptic dysfunction. J. Neurochem. *115*, 1215–1221.

Neuron, Volume *85*

Supplemental Information

Presenilin-1 **Knockin Mice Reveal Loss-of-Function Mechanism for Familial Alzheimer's Disease**

Dan Xia, Hirotaka Watanabe, Bei Wu, Sang Hun Lee, Yan Li, Evgeny Tsvetkov, Vadim Y. Bolshakov, Jie Shen, and Raymond J. Kelleher III

Supplemental Information

Presenilin-1 knockin mice reveal loss-of-function mechanism for familial Alzheimer's disease

Inventory of Supplemental Information

Supplemental Figures and Tables

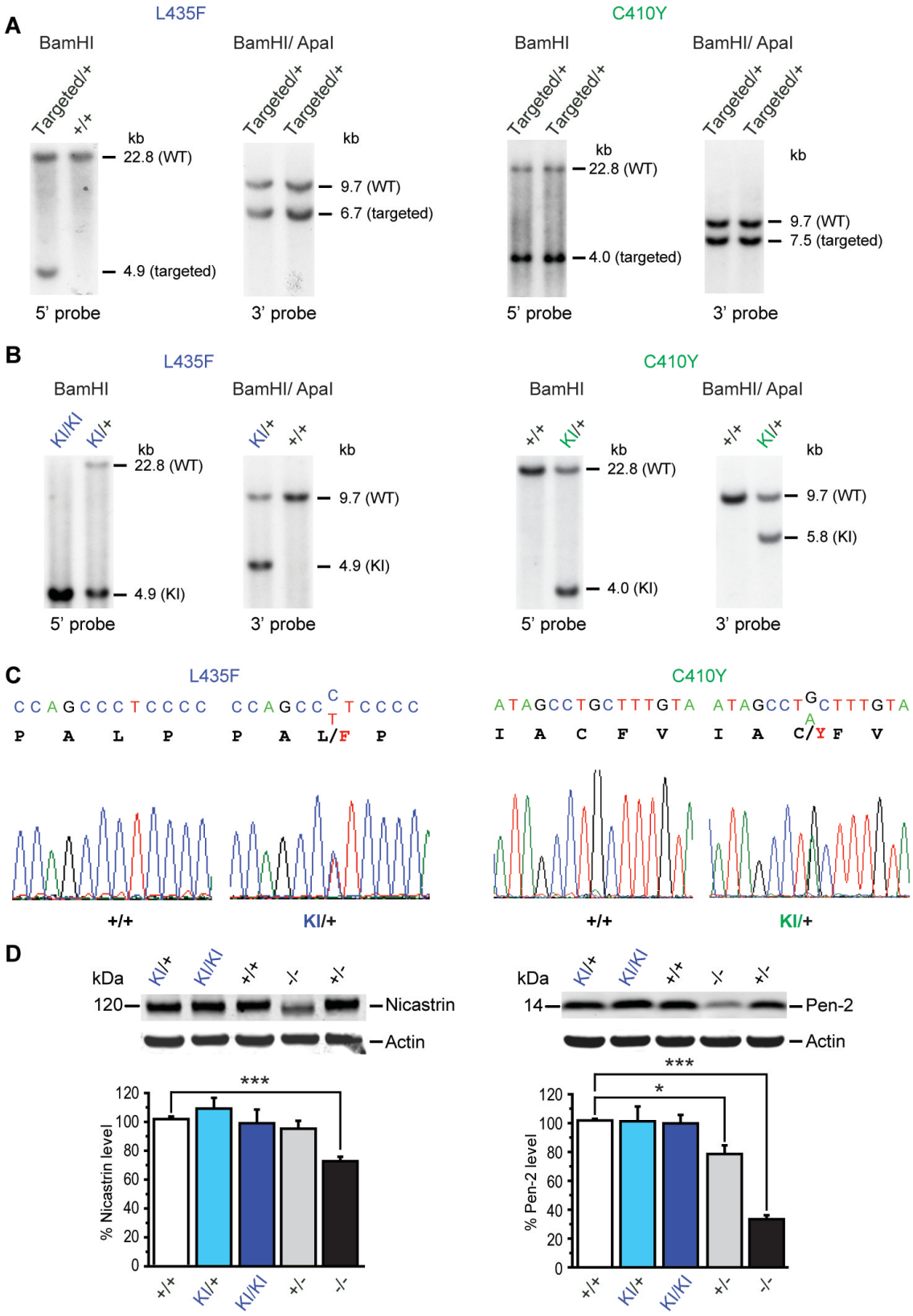

Figure S1. Confirmation of the L435F and C410Y KI Alleles in Genomic DNA and Characterization of Effects of the L435F Mutation on Other Components of the γ-Secretase Complex, Related to Figure 1

(A) Southern analysis of genomic DNA using both the 5' and the 3' external probes confirms the presence of the appropriate targeted alleles for the L435F and C410Y mutations in ES cell clones. For the L435F targeted mutation, genomic DNA from ES cells was digested with BamHI followed by Southern analysis using the 5' external probe. The resulting 22.8 kb band represents the wild-type allele, whereas the 4.9 kb band corresponds to the targeted allele. The targeting event was further confirmed by digesting ES cell genomic DNA with BamHI and ApaI followed by Southern analysis using the 3' external probe. The resulting 9.7 kb band represents the wild-type allele, whereas the 6.7 kb corresponds to the targeted allele. For the C410Y targeted mutation, genomic DNA from ES cells was digested with BamHI followed by Southern analysis using the 5' external probe. The resulting 22.8 kb band represents the wild-type allele, whereas the 4.0 kb band corresponds to the targeted allele. The targeting event was further confirmed by digesting ES cell genomic DNA with BamHI and ApaI followed by Southern analysis using the 3' external probe. The resulting 9.7 kb band represents the wild-type allele, whereas the 7.5 kb band corresponds to the targeted allele.

(B) Southern analysis of tail genomic DNA using the 5' and 3' external probes confirms the presence of the appropriate L435F and C410Y KI alleles following Cre-mediated excision of the *neo* cassette. For L435FKI mice, tail genomic DNA was digested with BamHI followed by Southern analysis using the 5' external probe. The resulting 22.8 kb band represents the wild-type allele, whereas the 4.9 kb band corresponds to the KI allele. The tail genomic DNA was then digested with BamHI and ApaI followed by Southern analysis using the 3' external probe. The resulting 9.7 kb band represents the wild-type allele, whereas the 4.9 kb corresponds to the KI allele. For C410Y KI mice, tail genomic DNA was digested with BamHI followed by Southern analysis using the 5' external probe. The resulting 22.8 kb band represents the wild-type allele, whereas the 4.0 kb band corresponds to the KI allele. The tail genomic DNA was then digested with BamHI and ApaI followed by Southern analysis using the 3' external probe. The resulting 9.7 kb band represents the wild-type allele, whereas the 5.8 kb band corresponds to the KI allele.

(C) Sequencing analysis of tail genomic DNA confirms the expected C to T substitution in L435F *KI*/+ mice and G to A substitution in C410Y *KI*/+ mice.

(D) In contrast to the reduction in levels of Nicastrin and Pen-2 in *Psen1*$^{-/-}$ brains at P0, levels of these γ-secretase components are normal in L435F *KI*/*KI* and *KI*/+ brains (n=4 per genotype).

Data are expressed as mean ± SEM. * $p < 0.05$; *** $p < 0.001$.

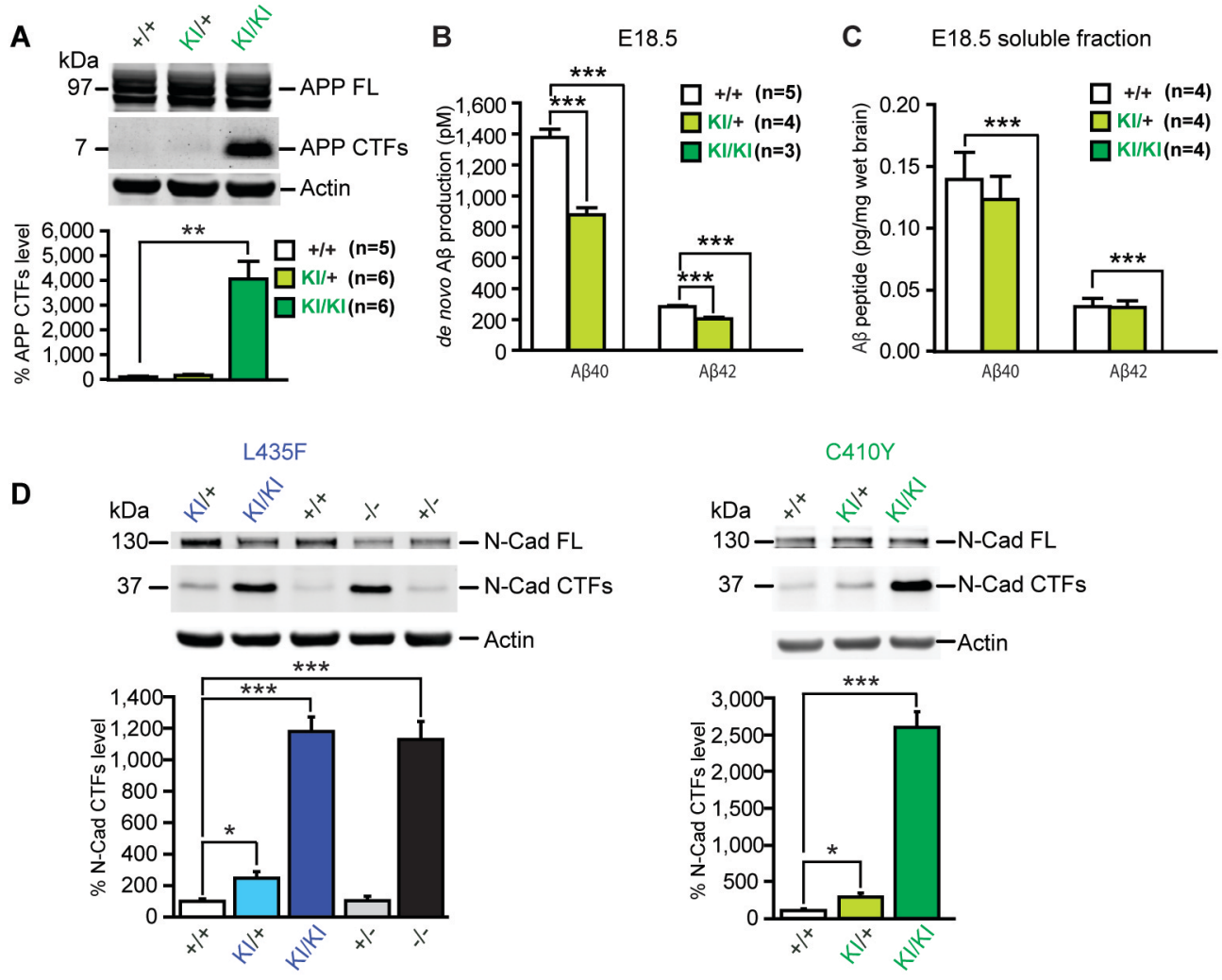

Figure S2. Abolished γ-Secretase Activity in C410Y *KI/KI* Brains, Related to Figure 3

(A) APP CTFs accumulate (~40-fold) in C410Y *KI/KI* brains relative to controls.

(B) ELISA measurements of Aβ40 and Aβ42 following *in vitro* γ-secretase assay. *De novo* production of Aβ40 and Aβ42 in C410Y *KI*/+ brains at E18.5 (n=4) is reduced by 36.2% and 27.3%, respectively, compared to *Psen1*$^{+/+}$ brains (n=5), whereas their production is undetectable in C410Y *KI/KI* brains (n=3).

(C) ELISA measurement of steady-state endogenous Aβ40 and Aβ42 from brain homogenates at E18.5. Levels of endogenous Aβ40 and Aβ42 are undetectable in C410Y *KI/KI* brains (n=4 per genotype).

(D) N-Cad CTFs accumulate (>10-fold) in L435F *KI/KI*, C410Y *KI/KI* and *Psen1*$^{-/-}$ brains, relative to controls (n=4 per genotype).

Data are expressed as mean ± SEM. * $p < 0.05$; **$p < 0.01$; *** $p < 0.001$.

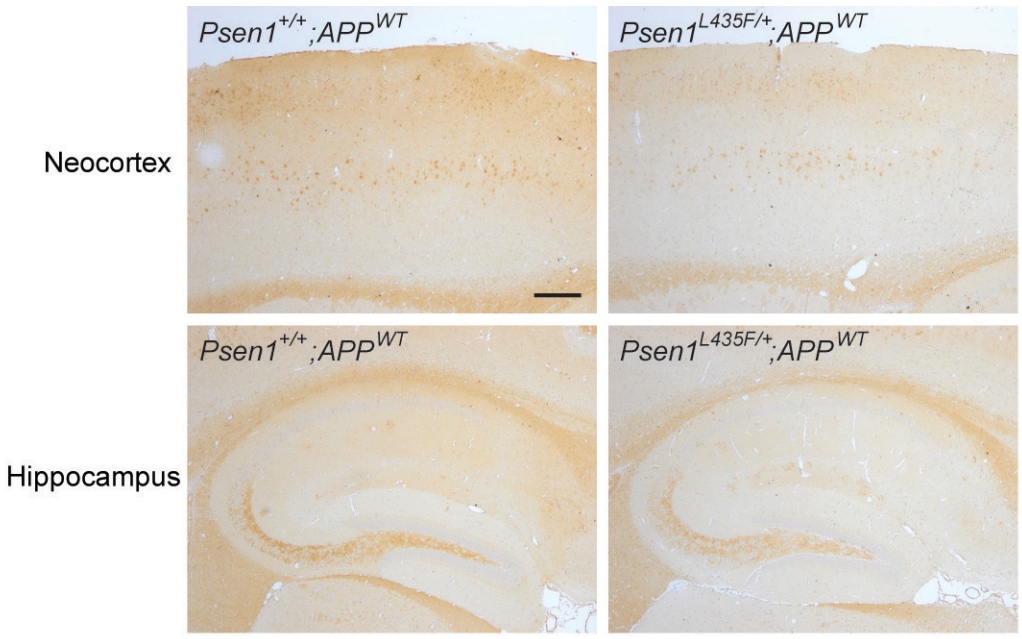

Figure S3. Absence of Amyloid Plaque Deposition in *Psen1*$^{L435F/+}$; *APP*^{WT} Mice, Related to Figure 4

No amyloid plaque deposition is detected in the cerebral cortex or the hippocampus of *Psen1*$^{L435F/+}$; *APP*^{WT} mice at the age of 18 months. Comparable brain sections were immunostained with an Aβ antibody (R1282) and counterstained with hematoxylin. Consistent with ELISA result, levels of Aβ are lower in *Psen1*$^{L435F/+}$; *APP*^{WT} mice compared to the control. Scale bar, 0.25 mm.

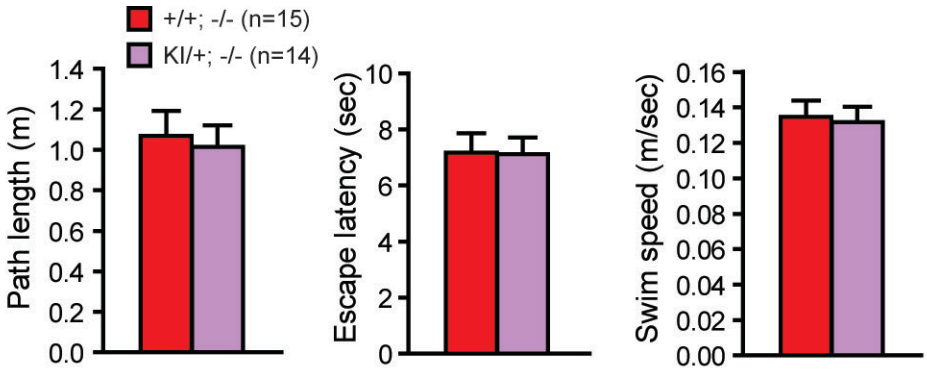

Figure S4. Normal Performance of *Psen1*$^{L435F/+}$; *Psen2*$^{-/-}$ Mice in the Visible Platform Version of the Water Maze Task, Related to Figure 5

No significant difference was observed between *Psen1*$^{L435F/+}$; *Psen2*$^{-/-}$ mice (n=14) and littermate *Psen1*$^{+/+}$; *Psen2*$^{-/-}$ mice (n=15) at 12 months of age in path length, escape latency and swim speed in the visible platform task. Data are expressed as mean ± SEM.

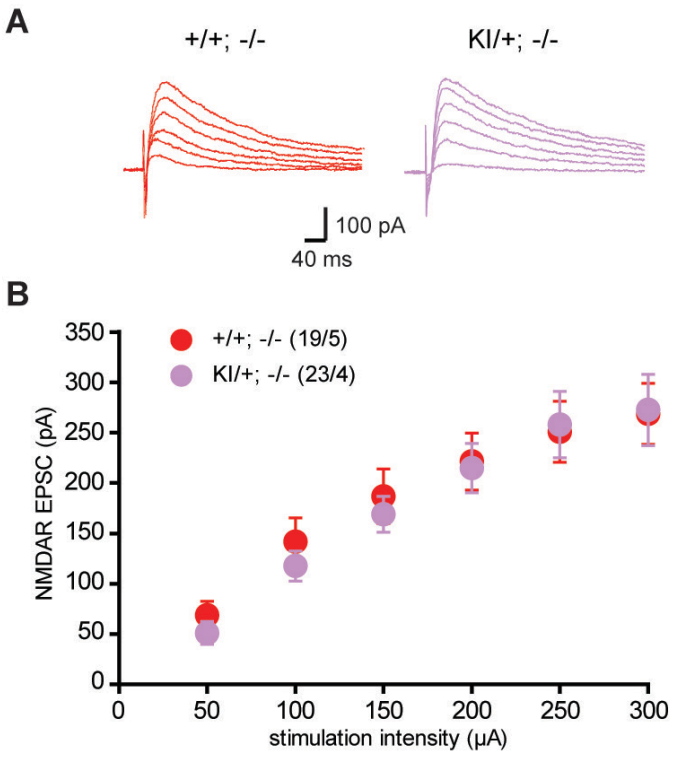

Figure S5. Normal NMDAR Responses in *Psen1*$^{L435F/+}$; *Psen2*$^{-/-}$ Mice, Related to Figure 6

(A) Pharmacologically isolated NMDAR EPSCs were evoked at Schaffer collateral-CA1 synapses by presynaptic stimuli of increasing intensity at a holding potential of +30 mV in acute hippocampal slices from *Psen1*$^{L435F/+}$; *Psen2*$^{-/-}$ and control mice. Traces are averages of 5 NMDAR EPSCs recorded in the presence of 10 μM NBQX.

(B) Input-output plots show similar NMDAR EPSCs between *Psen1*$^{L435F/+}$; *Psen2*$^{-/-}$ (n=23) and control (n=19) neurons (Two-way ANOVA, p = 0.9). The values in parentheses indicate the number of neurons (left) and mice (right) used in the analysis. Data are expressed as mean ± SEM.

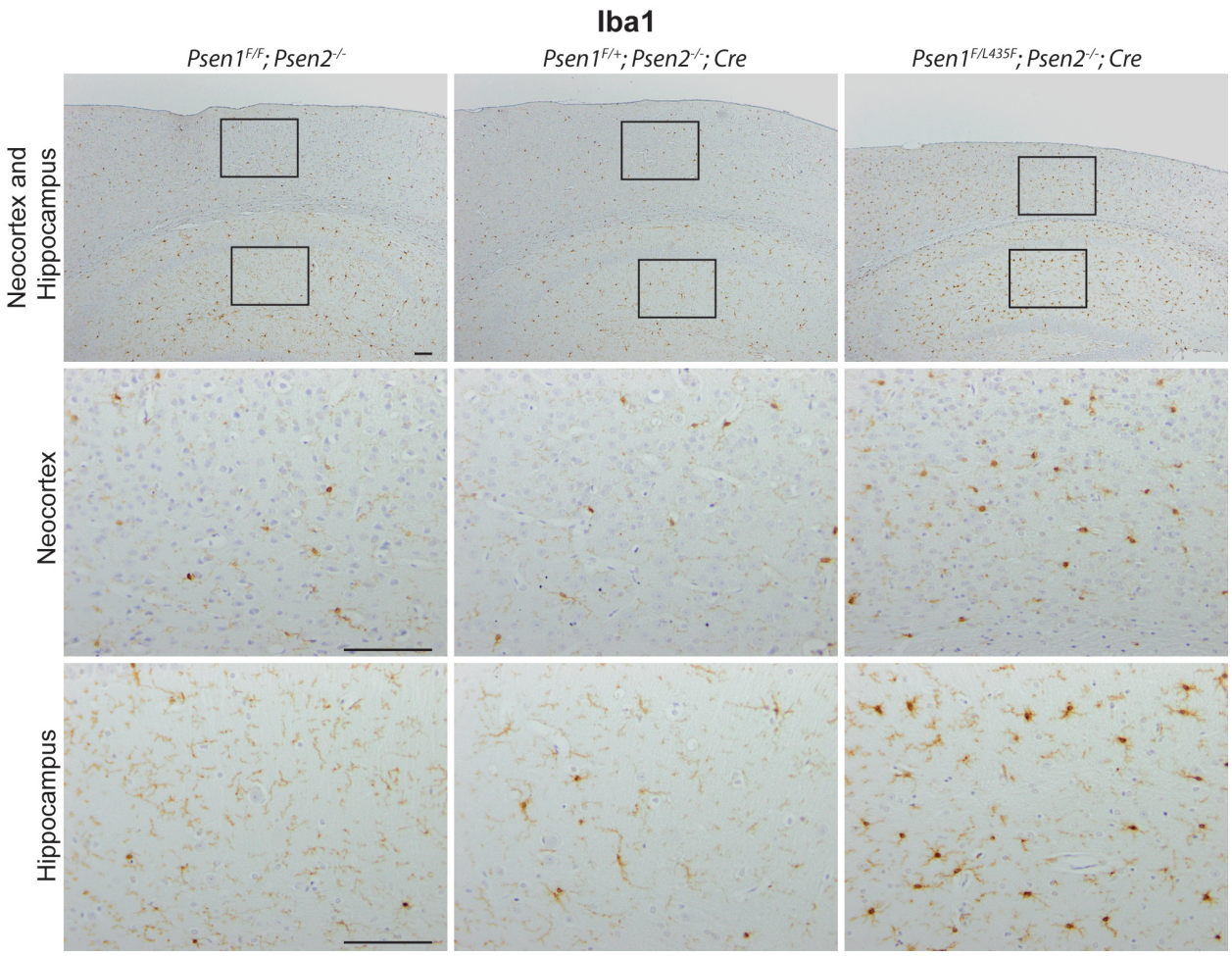

Figure S6. Microgliosis Associated with the L435F Mutation, Related to Figure 7

Immunohistochemical analysis for microglial specific marker Iba1 shows increased microglia in the neocortex and hippocampus of *Psen1*$^{F/L435F}$; *Psen2*$^{-/-}$; *Camk2a-Cre* mice at 12 months of age. Top: Overview of microgliosis in the neocortex and the hippocampus. Middle: Higher power views of the boxed neocortical area. Bottom: Higher power views of the boxed hippocampal area. Scale bar, 0.1 mm.

Table S1. Perinatal Lethality of L435F and C410Y *KI/KI* Mice, Related to Figure 1

	Genotype (L435F)		
Age	***+/+***	***KI/+***	***KI/KI***
E13.5	4	3	1
E14.5	7	5	2
E16.5	10	27	9
E18.5	13	24	9
P0	28	63	20
Percentage	25%	57%	18%
	Genotype (C410Y)		
Age	***+/+***	***KI/+***	***KI/KI***
E16.5	4	6	4
E17.5	3	7	6
E18.5	12	29	10
P0	19	31	12
Percentage	31%	50%	19%

The number of mice per genotype from E13.5 to P0 is shown. All newborn homozygous L435F and C410Y KI (*KI/KI*) pups died shortly after birth. The percentage of L435F *KI/KI* (~18%) and C410Y *KI/KI* (~19%) at P0 is lower than the expected Mendelian ratio (25%).

Table S2. Comparison of Mouse and Human Aβ40 and Aβ42 Levels in the Cortex of Various Genotypes, Related to Figure 3 and Figure 4

		Insoluble Aβ40	Fold	Insoluble Aβ42	Fold	Soluble Aβ40	Soluble Aβ42
mouse Aβ	*Psen1*$^{+/+}$ (n=7)	0.56 ± 0.02	1.0	0.72 ± 0.03	1.0	0.30 ± 0.03	0.09 ± 0.01
	Psen1$^{L435F/+}$ (n=10)	0.40 ± 0.01	0.7	0.60 ± 0.01	0.8	0.25 ± 0.04	0.11 ± 0.02
human Aβ	*Psen1*$^{+/+}$;*APP*^{WT} (n=4)	11.60 ± 0.44	20.7	3.10 ± 0.11	4.3	0.48 ± 0.08	0.24 ± 0.03
	Psen1$^{L435F/+}$;*APP*^{WT} (n=4)	8.54 ± 0.61	15.3	2.52 ± 0.18	3.5	0.18 ± 0.05	0.17 ± 0.05
	Psen1$^{+/+}$;*APP*^{MT} (n=4)	29.87 ± 0.96	53.3	30.65 ± 1.08	42.6	0.20 ± 0.04	0.61 ± 0.05
	Psen1$^{L435F/+}$;*APP*^{MT} (n=4)	23.34 ± 0.59	43.5	28.60 ± 1.72	39.7	0.21 ± 0.08	0.56 ± 0.07

Levels of endogenous mouse Aβ40 and Aβ42 and human Aβ40 and Aβ42 measured in insoluble and soluble fractions of cortical homogenates (expressed as pg/mg of wet brain) are shown. Samples were collected from *Psen1*$^{+/+}$ and *Psen1*$^{L435F/+}$ mice at 3 months of age, *Psen1*$^{+/+}$; *APP*^{WT} and *Psen1*$^{L435F/+}$; *APP*^{WT} mice at 9 months of age, and *Psen1*$^{+/+}$; *APP*^{MT} and *Psen1*$^{L435F/+}$; *APP*^{MT} *mice* at 2 months of age. Fold changes relative to *Psen1*$^{+/+}$ mice are also shown for insoluble Aβ40 and Aβ42. Data are expressed as mean ± SEM.

Supplemental Experimental Procedures

Generation of *Psen1* L435F and C410Y KI Mice

To determine the impact of FAD mutations *in vivo*, we generated two independent KI mice, in which the FAD-linked L435F and C410Y mutations were introduced into the genomic *Psen1* locus. Thus, these KI mice recapitulate precisely the genetic mutation in FAD patients with the mutant protein expressed under the control of the endogenous regulatory elements. For the L435F KI construct, a 3.2-kb left arm fragment and a 3.6-kb right arm fragment surrounding exon 12 were amplified by PCR using BAC genomic DNA (clone RP23–330F11, Children's Hospital Oakland Research Institute) as a template. The sequences of the primers used to PCR amply the left arm of the L435F KI targeting vector are 5'-CACTA*CCGCGG*TTGGTGTGGTAGCCAGCAC-3' and 5'-TCACTA*GCGGCCGC*AGTGCCAGGAGGTAAGTATGCACC-3' (the sequences for the *SacII* and *NotI* sites are italicized). The sequences of the primers used to PCR amply the right arm of the L435F KI targeting vector are 5'-CACTA*GTCGAC*TAGGAGGCTGAGGGAGAAAGATAC-3' and 5'-TCTCA*GATATC*CACAGACAGAACAAGCAGTCAAC-3' (the sequences of the *SalI* and *EcoRV* recognition sites are italicized). The L435F mutation was introduced into exon 12 by site-directed mutagenesis of the right arm fragment. The left and right arm fragments were then subcloned into the *PGKneolox2DTA* plasmid (gift of P. Soriano) to produce the L435F KI targeting vector. For the C410Y KI construct, a 2.8-kb left arm fragment and a 3.3-kb right arm fragment surrounding exon 11 were amplified by PCR using BAC genomic DNA (clone RP23–330F11) as a template. The primer sequences used to amplify the left arm of the C410Y KI targeting vector are 5'-CACTA*CCGCGG*GAGAAAAGTCGTGACTGTCTGC-3' and 5'-TCACTA*GCGGCCGC*CTCACAACTAACTACCCAAGG -3' (the italicized nucleotides indicate the sequences of the *SacII* and *NotI* sites). The primer sequences used to amplify the right arm of the C410Y KI targeting vector are 5'-CACTA*GTCGAC*GAGTTCTTAAGAGGTCTCCAGG-3' and 5'-TCTCA*GATATC*ACAGTACTCTTGTGTGACCC-3' (the italicized nucleotides indicate the sequences of

the *SalI* and *EcoRV* recognition sites). The C410Y mutation was introduced into exon 11 by site-directed mutagenesis in the left arm fragment. The left and right arm fragments were then subcloned into the *PGKneolox2DTA* plasmid (gift of P. Soriano) to produce the C410Y KI targeting vector.

To generate KI mice, the targeting vectors were linearized with SacII and electroporated into MKV6.5 ES cells (gift of R. Jaenisch), which were derived from C57BL/6 x 129 F1 hybrid mice. ES cells were maintained in medium supplemented with 150 μg/ml G418 (Invitrogen), and surviving clones were picked after 6 days of drug selection. ES cells were then screened for correct targeting events by Southern analysis. The same 5' and 3' external probes were used to screen and validate the proper recombination events for the generation of both L435F and C410Y KI alleles. Genomic DNA was purified from 231 independent ES clones derived from the L435F KI targeting event and 356 independent ES clones derived from the C410Y KI targeting event, digested with BamHI, and then subjected to Southern analysis using the 5'external probe. 105 L435F KI ES clones and 150 C410Y KI ES clones tested positive for proper homologous recombination in the left arm. 10 ES clones (2 for L435F and 8 for C410Y) containing the correct targeting event were expanded and further confirmed by Southern analysis using both the 5' and 3' external probes (BamHI for the 5' probe, ApaI and BamHI for the 3' probe). All 10 ES cell clones were confirmed to carry the correct homologous recombination events in both left and right arms. The probes were amplified from C57BL/6 x 129 F1 hybrid mouse tail genomic DNA. The primer sequences for the 5' external probe (516 bp) are 5'-AACAGGCTCTCCCTAGTAAG-3' and 5'-GCACTACATACATGTAGGCC-3', and the primer sequences for the 3' external probe (524 bp) are 5'-TCACAAGACATGGACCATCG-3' and 5'-AGGTTCAAGGTCATCCTTGG-3'.

For generation of each KI mouse, two independent ES cell clones (L435F: LF4-1-A and LF4-7-A; C410Y: CY4-7-D and CY4-7-F) that were confirmed to carry the correct homologous recombination events were injected into C57BL/6 blastocysts, and the resulting male chimeric mice were mated with C57BL6/J-129 F1 mice. Mice carrying the targeted allele were further crossed to *Camk2a-Cre* transgenic mice (Saura et al., 2004) to excise the floxed *PGK-neo* cassette in male germ cells. The resulting heterozygous KI mice were intercrossed to obtain homozygous KI mice for further characterization.

Correct heterozygous and Cre-mediated site-specific recombination events were confirmed by Southern analysis with tail genomic DNA using the external 5', 3', and the *neo* probes. Since offspring from both of the targeted ES cell clones for each KI mutation were indistinguishable, we used KI mice derived from a single ES clone for each mutation (L435F: LF4-7-A; C410Y: CY4-7-F) for further characterization. KI mice were maintained on the C57BL6/J-129 hybrid genetic background, and littermate controls were used for all analysis.

Psen1$^{L435F/+}$; *Psen2*$^{-/-}$ mice were generated by breeding *Psen1*$^{L435F/+}$mice with *Psen2*$^{-/-}$ mice (Steiner et al., 1999), which exhibited no detectable phenotypes. *Psen1*$^{L435F/+}$; *Psen2*$^{-/-}$ mice were further crossed with *Psen1*$^{F/F}$*; Psen2*$^{-/-}$*; Camk2a-Cre* mice, which were homozygous for the floxed *Psen1* (*Psen1*$^{F/F}$) and *Psen2*-null (*Psen2*$^{-/-}$) alleles, and hemizygous for the *Camk2a-Cre* transgene, to generate *Psen1*$^{F/L435F}$; *Psen2*$^{-/-}$*; Camk2a-Cre* mice. *Psen1*$^{F/L435F}$; *Psen2*$^{-/-}$*; Camk2a-Cre* mice were also maintained by crossing with *Psen1*$^{F/F}$*; Psen2*$^{-/-}$ mice. *Psen1*$^{KI/+}$*; APP*^{WT} and *Psen1*$^{KI/+}$*; APP*^{MT} mice were generated by crossing *Psen1*$^{L435F/+}$ mice to human APP wild-type (*APP*^{WT}, I5 line) or mutant (*APP*^{MT}, J20 line) transgenic mice (Mucke et al., 2000).

All animal procedures were approved by and conducted in accordance with the guidelines of the Institutional Animal Care and Use Committees.

Northern analysis

Total RNA was extracted from brains of E18.5 or P0 pups using TRI reagent (Sigma). 16 μg total RNA per genotype was separated on formaldehyde agarose gels and transferred to nylon membranes. Probes were synthesized using Prime-It II random labeling kit (Stratagene) and then used for membrane hybridization at 50° C overnight. The primer pairs used in this study were as follows: 5'-TGCACCTTTGTCCTACTTCC-3' and 5'-ATGACACTGATCATGATGGC-3' for *Psen1*, 5'-CAGTCCCAAGGAGAAAAACC-3' and 5'-CAGCAGCAGCCTTAGCGGAG-3' for *Hes5*. Hybridization was performed using [α-^{32}P] dCTP-labeled probes specific for each gene. NIH Image

software was used to quantify the level of transcripts by comparing the intensities of the bands after subtracting the background.

Western analysis

Dissected brains were homogenized in RIPA buffer (50 mM Tris-Cl (pH 7.6), 150 mM NaCl, 0.5 mM EDTA, 1% NP40, 0.5% sodium deoxycholate, 0.1% SDS, protease inhibitor cocktail (Sigma), 1mM PMSF). Proteins were separated in NuPAGE gels (Invitrogen) and transferred to nitrocellulose membranes. Primary antibodies were rabbit anti-PS1 NTF (Calbiochem), mouse anti-PS1 CTF (Millipore), rabbit anti-Pen2 (Zymed), rabbit anti-Nicastrin (Sigma), rabbit anti-Actin (Sigma), rabbit anti-Notch1 (Val1744) (Cell Signaling), mouse anti-SNAP25 (Millipore), rabbit anti-APP (C8; gift of D. Selkoe) and mouse anti-GFAP (Sigma). Membranes were then incubated with dye-coupled secondary antibodies (goat anti-rabbit IRdye800, goat anti-mouse IRdye680, goat anti-rabbit IRdye680, and goat anti-mouse IRdye800 from Licor). Signals were quantified with the Odyssey Infrared Imaging System (LI-COR Bioscience).

***In vitro* γ-secretase assay**

γ-secretase-mediated *de novo* Aβ generation was measured using a method described previously (Watanabe et al., 2012). Briefly, 1% CHAPSO-solubilized microsomal fractions from E18.5 brains or adult cortices at 3 months of age were mixed with the assay buffer (final concentration of reaction system: 150 μg/ml γ-secretase fraction, 0.3% CHAPSO, 10 mM HEPES (pH 7.3), 150 mM NaCl, 1 mM EDTA, complete protease inhibitor cocktail (Roche), 5 mM 1,10-phenanthroline, 5 mg/ml phosphoramidon, and 0.1% (w/v) phosphatidylcholine), and incubated with 1-2 μM recombinant C100-FmH (substrate for *de novo* Aβ generation) or N102-FmH (substrate for *in vitro* NICD production) at 37° C for 14 hr. 7.5 μg and 15 μg CHAPSO-solubilized microsomal fractions were used for *de novo* Aβ generation and NICD production, respectively. To quantify *de novo* Aβ generation, samples were subjected to ELISA specific for Aβ40 and Aβ42. Specific γ-secretase activity was obtained by subtracting the values obtained from a reaction conducted in the presence of γ-secretase inhibitor (III-31C, 2 μM, Sigma). For Western analysis

of *in vitro* γ-secretase assay (NICD production), levels of cleaved substrate (NICD) were normalized to levels of SNAP25. For recombinant C100-FmH and N102-FmH, which are tagged with Flag-Myc-Histidine, bacterial strain DH5α was transformed with pTrcHis2A-C100-FmH and pTrcHis2A-N102-FmH plasmids, respectively, and induced with 0.1 mM IPTG for 3 hours. Each recombinant protein was purified over a Ni^{2+}-chelated HiTrap Chelating HP column (Amersham).

Enzyme-linked Immunosorbent Assay (ELISA)

For *de novo* Aβ ELISA, monoclonal antibodies directed against the C terminus of Aβ40 (Covance; 11A50-B10) or Aβ42 (Covance; 12F4) were used as specific capture antibody. A biotinylated monoclonal secondary antibody (Covance; 4G8) recognizing Aβ residues 17–24 was used for detection of both Aβ40 and Aβ42 with a reporter system of streptavidin-conjugated alkaline phosphatase (Promega) and AttoPhos reagent (Promega). Fluorescence was measured by excitation at 444 nm and emission at 555 nm by a Wallac 1420 spectrometer (PerkinElmer). Aβ40 and Aβ42 synthetic peptide standards (BioPeptide Inc.) were included in each analysis to quantify Aβ levels, which were expressed as the concentration in pM of Aβ40 or Aβ42.

For mouse endogenous and human Aβ ELISA, mouse embryonic brains or adult cortices were homogenized with 5 volumes of TBS or 0.2% diethylamine (DEA) and centrifuged at 175,000 x *g* for 30 min. The supernatants (neutralized by 0.5 M Tris-Cl, pH 6.8 when using DEA) were used as soluble fractions for Aβ measurement. The pellet was washed with TBS and resuspended in an equal volume of 5 M guanidine-HCl, 50mM Tris-HCl, pH 8.0 and rotated at room temperature overnight. The GuHCl suspensions were used as insoluble fraction and diluted by 1% blocking solution (MesoScale Discovery, MSD) for Aβ measurement. The mouse Aβ (1-40) and Aβ (1-42) peptide standards were purchased from Ana Spec Inc. The human Aβ (1-40) and Aβ (1-42) peptide standards were included in the MSD kit. Soluble and insoluble fractions were subjected to MSD 96-well MULTI-SPOT Human/ Rodent (4G8) Abeta Triplex Ultra-sensitive Assay (MesoScale Discovery) for Aβ measurement. The ELISA reactions were read using the SECTOR Imager 2400A.

Behavioral analysis

Mice were housed in a standard 12 hr. light-dark cycle. Only male mice were used in behavioral studies, and the experimental groups were always tested with littermate controls. The experimenter was blind to the genotypes of the mice.

Hidden platform water maze task and pattern completion test

The Morris water maze is a circular pool 160 cm in diameter. Cohorts of naïve *Psen1*$^{L435F/+}$; *Psen2*$^{-/-}$ and control mice at 12 months of age were trained in the hidden platform version of the task for a total of 14 days. The release point for each training trial was varied among all four quadrants in a pseudorandom manner. Four distal visual cues were placed on the walls during training and full-cue probe tests, whereas three of the cues were removed for the partial-cue probe test. The escape platform (10 cm in diameter) was submerged ~1 cm beneath the water surface and maintained in a constant position. Mice received four training trials daily with a maximum duration of 90 sec. and an inter-trial interval of 15 min. Mice that did not locate the platform during a training trial were guided to the platform and allowed to remain on it for 15 sec. Location of mice in the pool was continuously monitored using an automated tracking system (HVS Image).

After 6 days and 12 days training, probe tests were performed on the mornings of days 7 and 13 prior to administering new training trials. Probe tests were conducted by removing the hidden platform, releasing mice from the opposite quadrant, and allowing them to search for the platform location for 90 sec. Upon completion of the probe tests, the platform was re-installed in the same position and four new training trails were administered.

After 13 days of training, a partial-cue probe test was administered on the morning of day 14 to assess pattern completion. After completion of the hidden platform water maze task, the visible-cue version of the task was performed to verify visual and swimming ability by administering four trials with the platform position marked by a yellow object. The genotypic effect on escape latency during the 14-day training was assessed by two-way ANOVA ($F=8.06$; $df=1, 27$; $p=0.0046$) using Prism 6.

Radial arm maze

Five days prior to starting the task, mice were singly housed and fed restrictively to reduce their body weight to 80-85% of their free-feeding weight (Dillon et al., 2008). The food restriction regimen was maintained throughout the training and testing period. The radial arm maze was performed on an apparatus consisting of eight arms (33 cm long x 5.5 cm wide, equally spaced at 45° angles) and a central platform (27 cm diameter). Eight vertical doors (transparent Plexiglas) at the junction of the arms and central platform could be remotely raised and lowered by the experimenter. The maze was place in a well-lit room with four distal visual cues on the walls. Cohorts of naïve *Psen1*$^{L435F/+}$; *Psen2*$^{-/-}$ and littermate control mice (n=9-10 each) at 18 months of age were used.

On the first 2 days (habituation sessions), mice were allowed to explore the maze freely and eat 20-mg casein pellets scattered in the whole maze (1 in each food cup, 1 in the middle of each arm, and 3 in the central platform). Habituation session ended when the mouse consumed all pellets or a maximum time of 15 minutes had elapsed.

Following 2 days of habituation, mice were subjected to 8 days of training in a spatial discrimination version of the task. Animals were brought to the ante-room to acclimate on the transport rack for at least 30 minutes. During training sessions, three arms of the maze were baited (arm 3, 4 and 8) and 1 casein pellet was placed in a food cup in each baited arm. The baited arms were maintained in a consistent location and orientation with regard to the distal visual cues throughout the experiment. Each mouse was subjected to 6 consecutive training trials every day with an inter-trial interval of 1–2 minutes. During each trial, a mouse was placed on the central platform and allowed to explore the arms until it had retrieved the food pellets from the three baited arms or a maximum time of 5 minutes had elapsed. Re-entries were prevented by lowering each arm's door after a mouse had visited that arm and returned to the central platform. The maze was randomly rotated and cleaned with alcohol between trials, to prevent the use of olfactory cues from one trial to another. A reference memory (RM) error was defined as a visit to a non-baited arm during any trial (range 0-5), with a maximum of five per trial. The order of arm entries was recorded and analyzed throughout training to determine the number of 45° turns between two arms

successively visited and the percentage of 45° turns was used as an index of non-spatial search strategy. A stopwatch was used to record the task completion time for each trial.

Two-way ANOVA revealed that both genotypic groups required similar amounts of time to complete the trial during the 8-day training session ($F=1.18$; $df=1, 17$; $p=0.2786$), and that there was a significant genotypic effect on reference errors ($F=4.59$; $df=1, 17$; $p=0.0325$) and percentages of 45 degree turns ($F=13.63$; $df=1, 17$; $p=0.0002$).

Field and whole-cell electrophysiological analysis

All field and whole-cell electrophysiological recordings were performed on naïve *Psen1*$^{LA435F/+}$; *Psen2*$^{-/-}$ and control mice at 6 months of age. Acute hippocampal slices (400 μm) were prepared as described (Zhang et al., 2009). Slices were maintained in a storage chamber containing aCSF (125 mM NaCl, 3 mM KCl, 1.25 mM NaH_2PO_4, 1 mM $MgCl_2$, 2 mM $CaCl_2$, 25 mM $NaHCO_3$, 10 mM dextrose, 1.2 mM pyruvate and 0.4 mM Na-ascorbate, pH 7.4 (300 ± 5 mOsm) saturated with carbogen (95% O_2 and 5% CO_2) at 30° C. Stimulation (200 μs) pulses were delivered with a bipolar concentric metal electrode. Synaptic strength was quantified as the initial slope of field potentials recorded with aCSF-filled microelectrodes (1 to 2 MΩ). Data were analyzed using Clampfit (Molecular device). Synaptic facilitations were measured as the percentage of the fEPSP slope relative to the initial fEPSP slope of a given stimulus train in individual slices.

For LTP recordings at the recurrent commissural/associational (C/A)-CA3 synapses, a bipolar stimulation electrode was placed in the CA3 stratum radiatum to stimulate C/A fibers, and C/A field potentials were recorded in the CA3 stratum radiatum. Baseline responses were collected every 15 sec. using a stimulation intensity that yielded 60% of the maximal response. LTP was induced by 3 trains of high-frequency stimulation (HFS: 1 sec.-trains of 100 Hz tetanization every 10 sec.). Average responses (mean ± SEM) are expressed as percentage of the pre-HFS baseline response. Since group II mGluR agonists selectively block mossy fiber-CA3 responses (Kamiya et al., 1996), group II-selective mGluR

agonist (2S,1'R,2'R,3'R)-2-(2,3-dicarboxycyclopropyl) glycine (DCG-IV; 2 μM) was applied at the conclusion of the experiment to confirm that C/A-CA3 synaptic responses were analyzed.

Whole-cell recordings of evoked EPSCs were obtained from pyramidal neurons in the CA1 region under visual guidance (DIC/ infrared optics) with an EPC-10 amplifier and Pulse v8.67 software (HEKA Elektronik). Isolated NMDAR EPSCs were recorded in the presence of 10 μM NBQX in the external solution. Patch electrodes (3-4 MΩ) contained (in mM): 135 Cs-methane-sulfonate, 5 NaCl, 1 $MgCl_2$, 0.2 EGTA, 10 HEPES, 2 MgATP, and 0.1 NaGTP (adjusted to pH 7.2 with CsOH). Synaptic responses were evoked (at 0.05 Hz) by stimulation of Schaffer collaterals with a concentric stimulation electrode (Tsvetkov et al., 2002) positioned in the stratum radiatum. Synaptic currents were filtered at 1 kHz and digitized at 5 kHz. The EPSC amplitude was measured as the difference between the mean current over a 1–2-ms window at the response peak and the mean current during a prestimulus baseline. In LTP experiments, the EPSCs were recorded at a holding potential of –70 mV. For induction of LTP, 80 presynaptic stimuli were delivered at 5 Hz to the Schaffer collaterals, paired with postsynaptic depolarization to +30 mV. Summary LTP graphs were constructed by normalizing data in 60 s epochs to the mean value of the baseline EPSC amplitude. The magnitude of LTP was estimated in a time window of 5 min at 45 – 50 min post-induction. Results are shown as mean ± SEM. All electrophysiological analysis was performed in a genotype blind manner using littermate mice at 6 months of age.

Histological analysis

Embryos at E16.5 were dissected, and the tail and limbs were removed from each embryo for genotyping. Embryonic heads were then removed and fixed in 4% paraformaldehyde for 3 hours at 4° C. Brains were dissected and embedded in paraffin, and transverse sections were serially cut at 10 μm. For HE staining, every fifth section was deparaffinized, dehydrated, and stained with 0.5% hematoxylin and 1% eosin, and comparable sections from both genotypic groups were analyzed. For immunohistochemical analysis, sections were deparaffinized, dehydrated, blocked with a solution containing 5% normal goat serum and 0.1% BSA for 1 hr. at room temperature, and incubated with anti-Ki67 antibody (1:200; Novocastra)

overnight at 4° C. Following PBS washes, sections were incubated with appropriate Alexa Fluor 488-conjugated secondary antibodies (Molecular Probes). The number of Ki67-immunoreactive cells was quantified using 4 comparable sections per brain and 4 brains per genotype. Images were captured with a LSM 510 confocal microscope (ZEISS).

Adult brains were perfused with PBS, fixed in 4% PFA, processed for paraffin embedding, and serially sectioned (10 μm). For stereological analysis, adult brain sections were stained with 0.5 % cresyl violet (Nissl) or immunostained with antibody against NeuN (1:300; Millipore), cleaved Caspase-3 (1:100, Cell Signaling Technology), GFAP (1:500; Sigma), Iba1 (1:250; Wako), or Aβ (1:1000; R1282). Cortical volume and neuron number were estimated using the fractionator and optical dissector methods under an Olympus BX51 light microscope equipped with a CCD camera connected to a computer running Bioquant image analysis software. For immunostaining in adult brain, brain sections were incubated with biotinylated secondary antibodies and developed by using the peroxidase avidin–biotin reagent and the Vectastain Elite ABC kit (Vector Laboratories). For TUNEL staining, the deparaffinized and rehydrated brain sections were immersed in 10 mM citrate buffer (pH 6.0) and boiled in a microwave oven for antigen retrieval. Slides were blocked in 20% of goat serum for 60 min followed by treatment with fluorescein (Roche) at 37° C for 1 hr. The slides were then washed in TBS, and TUNEL staining was visualized for analysis using a Leica DMI6000 Microscope.

Supplemental References

Dillon, G.M., Qu, X., Marcus, J.N., and Dodart, J.C. (2008). Excitotoxic lesions restricted to the dorsal CA1 field of the hippocampus impair spatial memory and extinction learning in C57BL/6 mice. Neurobiol Learn Mem 90, 426-433.

Kamiya, H., Shinozaki, H., and Yamamoto, C. (1996). Activation of metabotropic glutamate receptor type 2/3 suppresses transmission at rat hippocampal mossy fibre synapses. J Physiol 493 (Pt 2), 447-455.

Mucke, L., Masliah, E., Yu, G.Q., Mallory, M., Rockenstein, E.M., Tatsuno, G., Hu, K., Kholodenko, D., Johnson-Wood, K., and McConlogue, L. (2000). High-level neuronal expression of abeta 1-42 in wild-type human amyloid protein precursor transgenic mice: synaptotoxicity without plaque formation. J Neurosci 20, 4050-4058.

Saura, C.A., Choi, S.Y., Beglopoulos, V., Malkani, S., Zhang, D., Shankaranarayana Rao, B.S., Chattarji, S., Kelleher, R.J., 3rd, Kandel, E.R., Duff, K., *et al*. (2004). Loss of presenilin function causes impairments of memory and synaptic plasticity followed by age-dependent neurodegeneration. Neuron 42, 23-36.

Steiner, H., Duff, K., Capell, A., Romig, H., Grim, M.G., Lincoln, S., Hardy, J., Yu, X., Picciano, M., Fechteler, K., *et al*. (1999). A loss of function mutation of presenilin-2 interferes with amyloid beta-peptide production and notch signaling. J Biol Chem 274, 28669-28673.

Tsvetkov, E., Carlezon, W.A., Benes, F.M., Kandel, E.R., and Bolshakov, V.Y. (2002). Fear conditioning occludes LTP-induced presynaptic enhancement of synaptic transmission in the cortical pathway to the lateral amygdala. Neuron 34, 289-300.

Watanabe, H., Xia, D., Kanekiyo, T., Kelleher, R.J., 3rd, and Shen, J. (2012). Familial frontotemporal dementia-associated presenilin-1 c.548G>T mutation causes decreased mRNA expression and reduced presenilin function in knock-in mice. J Neurosci 32, 5085-5096.

Zhang, C., Wu, B., Beglopoulos, V., Wines-Samuelson, M., Zhang, D., Dragatsis, I., Sudhof, T.C., and Shen, J. (2009). Presenilins are essential for regulating neurotransmitter release. Nature 460, 632-636.